Effect of density and unit cell size grading on the stiffness and energy absorption of short fibre-reinforced functionally graded lattice structures

János Plocher, Ajit Panesar*

Department of Aeronautics, Imperial College London, SW7 2AZ, UK

email: * a.panesar@imperial.ac.uk

ABSTRACT

Architectured structures, particularly functionally graded lattices, are receiving much attention in both industry and academia as they facilitate the customization of the structural response and harness the potential for multi-functional applications. This work experimentally investigates how the severity of density and unit cell size grading as well as the building direction affects the stiffness, energy absorption and structural response of additively manufactured (AM) short fibre-reinforced lattices with same relative density. Specimens composed of tessellated body-centred cubic (BCC), Schwarz-P (SP) and Gyroid (GY) unit cells were tested under compression. Compared to the uniform lattices of equal density, it was found, that modest density grading has a positive and no effect on the total compressive stiffness of SP and BCC lattices, respectively. More severe grading gradually reduces the total stiffness, with the modulus of the SP lattices never dropping below that of the uniform counterparts. Unit cell size grading had no significant influence on the stiffness and revealed an elastomer-like performance as opposed to the density graded lattices of the same relative density, suggesting a foam-like behaviour. Density grading of bending-dominated unit cell lattices showcased better energy absorption capability for small displacements, whereas grading of the stretching-dominated counterparts is advantageous for large displacements when compared to the ungraded lattice. The severity of unit cell size graded lattices does not affect the energy absorption capability. Finally, a power-law approach was used to semi-empirically derive a formula that predicts the cumulative energy absorption as a function of the density gradient and relative density. Overall, these findings will provide engineers with valuable knowledge that will ease the design choices for lightweight multi-functional AM-parts.

***Keywords*:** Functionally grading; Lattices; Material Extrusion; Lightweight Structures, Composites

1 Introduction

As the industry is increasingly employing architectured structures in the design for additive manufacturing in recent years, aspects of structural performance and response are progressively emerging at the forefront of academic research. Additive manufacturing (AM) has made latticing a viable lightweighting practice that is increasingly being adopted in the product design process to-date [1]. Having the ability to produce intricate structures with ease, opens new possibilities for the design and structural optimisation and therefore sets AM into the position of being a serious alternative to conventional manufacturing techniques like CNC

machining. Hence, a number of useful application have been presented for the biomedical sector [2–4], aerospace [5] or consumer products [6,7].

Simultaneously, the AM-industry is - among others - benefitting from a growing pallet of print materials [8], pushing the boundaries of intrinsic mechanical properties and hence progressing towards industrial production. Particularly for fused deposition modelling (FDM) processes, short and continuous fibre-reinforced (FR) filaments offer yet another means of improving the specific stiffness [9–17]. As the performance is a function of the fibre length and orientation [15], which in FDM is dictated by print direction [15,18–21], the inherent porosity in a layered structure, compromising the performance, can be offset to even match the performance of FR compression moulded parts [15].

In contrast to foams, representing an unstructured (i.e. stochastic structures) geometry, AM lends itself for fabricating periodically-controlled cellular structures with repeating unit cells. These types of lattices, commonly composed of either strut- or surface-based unit cells like e.g. the implicitly defined Triply Periodic Minimal Surfaces (TPMS), has immediate benefits for multiphysics problems. Compared to continuum solid solutions, they provide - inter alia - a good strength-to-weight ratio [22–24], greater energy absorption and damping capabilities [25–31], enable partial permeability or improved thermal conduction [32–35], in exchange for a reduced stiffness. Hence, they are particularly suitable for multi-objective optimisations, yielding parts with functional integration in which the geometrical configuration has more than a structural purpose.

As functional graded lattices (FGLs) are recently not only receiving much attention in research [36,37] but also in industry through more readily available modelling software like *nTopology* [38], *Altair* [39] or *Materialise* [40], specifically tailored solutions, providing a carefully weighted trade-off between structural and functional performance, become even more tangible. From a practical standpoint, AM enables us to manufacture FGLs with ease, providing the capability to create structures with a microstructural, composition and porosity gradient, as reviewed in detail in [4]. Previous works have studied aspects of modelling [33,36,41–46] as well as manufacturing and testing [2,37,45–48] to explore the mechanical properties of such architected structures. Most studies to-date, conducting finite element analyses, are limited to linear-elastic investigations, whereas models predicting the behaviour beyond the yield point, as shown e.g. in [49], would be more valuable for understanding the behaviour of FGLs. The key to fathom the underlying mechanisms and improve these models in the future are experimental investigations.

Fundamental insights have been offered through comparison between the compressive performance of uniform and graded lattices composed e.g. graded strut- [37,47,48,50,51] or TPMS-based lattices [2,52,53]. A major conclusion from most of these initial studies was an improved energy absorption capability [37,47,48,50,52] of the graded over the ungraded lattices of the same density and progressive failure of unit cell regions, often exhibiting 45° shear band failure [2,48,54] in rigid polymers or metal specimens. Yang et al. [55] have also conducted research into the failure of specimens tested transverse to the gradient direction and found a similar behaviour as the uniform counterparts with favourable stiffness and strength values over specimens tested parallel to the density gradient. Recently, light was also shed on

the failure behaviours induced by differently radially graded lattices [49] as well as the potential of this type of grading to outperform uniform lattices both in terms of mechanical performance and permeability [56]. So far only little research was focusing on the aspects of strength in FGLs [53,57] and the effective rather than nominal stiffness of FGLs. Besides being partly limited by a step-wise rather than true linear gradient or a sole comparison between a graded and a uniform lattice, studies have yet to provide an in-depth understanding about the effect of e.g.: 1) Severity of grading, 2) Strut- vs surface-based lattices, 3) Print materials, 4) Manufacturing, etc. on the overall performance. Regarding the evaluation of the effective stiffness of FGLs, studies have made use of the Voigt model [53,55,57], however the assumption of a continuous change in stiffness as a function of the gradient direction, as proposed in [41], is likely more accurate for truly linearly graded specimens.

Another increasingly investigated type of architected structures utilize morphing approaches to realize a smooth transition between boundaries of e.g. dissimilar unit cell sizes or unit cell types. Yang et al. [58] have presented two methods to achieve the required hybridisation i.e. morphing of TPMS lattices, by employing a Sigmoid function or a Gaussian radial basis function in order to connect two or multiple cell type regions, respectively. Similarly, Yoo and Kim [59] demonstrated how such TPMS-based multi-morphology structures can be achieved through the use of a volumetric distance field and beta growth functions. By changing the morphology locally, these structures lend themselves for precisely customizing the mechanical performance alongside e.g. permeability or heat conduction, paving the way for even more advanced engineering solutions. Despite the tools, making the modelling of these lattices feasible, only little experimental investigations were conducted yet [60].

For an increased application of FGLs in industry, databases will be required to build confidence in predicting their performance [61]. How to use, classify and apply architected structures has recently been discussed in [62,63]. Central to answering this question is to identify all the individual influencing variables that can be altered and create experimentally or numerically derived datasets that allow us to provide better consultancy when it comes to designing effectively for AM. This work sits at the core of this question and aims at answering the question of "how the severity of grading and build direction relates to the stiffness and energy absorption response of FGLs".

More specifically, this work seeks to experimentally investigate how the severity of density and unit cell size grading affects the mechanical performance of lattices with the same relative density tested in compression. In view of DfAM constraints, the effect of the printing direction i.e. prevailing fibre direction on the properties is also elucidated for the density graded lattices. The properties of ungraded (i.e. uniform density from one unit cell to another) lattices with various densities have been obtained to derive trends i.e. apply scaling laws for the density graded FGLs. Moreover, the ungraded lattice of the same relative density functioned as reference for the FGLs. Both the stiffness and the energy absorption behaviour are the key performance parameters investigated in both types of FGLs. The properties were compared in part to other engineering materials as well as ideally bending- and stretching dominated behaviour, following the categorization of Gibson-Ashby. Predictions for the stiffness of

lattices with higher fibre volume fraction were made using the Halpin-Tsai criterion. Semi-empirical energy absorption curves were derived with respect to unit cell type and severity of grading. Moreover, the remit of this work includes providing insight into the failure mechanisms/ structural response. Overall, this work provides valuable guidelines for the design of fibre-reinforced FGLs and sheds light on the potential of grading for functional lightweight AM-parts.

The outline of the paper is as follows. First, the design-to-test procedure is outlined in the methodology, constituting everything from the fundamentals for creating the FGLs to the approaches for assessing their mechanical performance. Secondly, the results of the compression tests are presented for both baseline (ungraded) and graded specimens. Subsequently, these are discussed considering the observed structural response/failure and recorded performance before concluding by summarizing the main findings and providing an outlook.

2 Methodology

The methodology of this work is comprised of the design-to-test workflow illustrated in Fig. 1. The work is hereby limited to short-fibre reinforced nylon as the print material and cubic tests specimens with an edge length of 30 mm for both density and unit cell size graded lattices. The former set of specimens is composed of 6x6x6 unit cells, whereas the latter is made up of a constant initial 3x3 unit cell arrangement at the bottom and increases smoothly into up to 9x9 unit cells per layer.

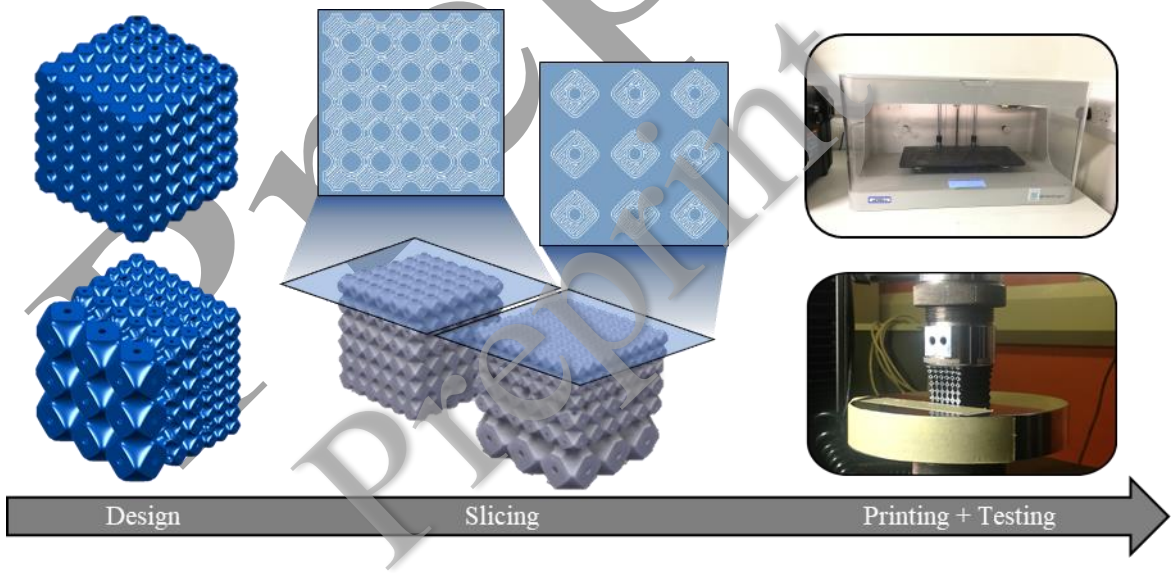

Fig. 1: Overview of the methodology followed for investigating the mechanical performance of FGLs.

2.1 Functionally graded lattice structures

The approach for generating the density graded lattice structures is based on the work of Panesar et al. [36], which allows a true functionally governed grading, and the method for the unit cell size grading was obtained from Yang et al. [58]. Both functionalities were

implemented into the in-house software *LatTess* (Lattice Tessellation), developed upon [33,36] by Panesar and co-workers, which served as a means of creating the FGLs in this work.

In the case of the TPMS lattices, the geometric surface representation is hereby defined as an implicit trigonometric function

$$f(x,y,z) \leq t \quad \text{(Eq.1)}$$

, whereby the isovalue *t* serves as a control parameter for the offset from the zero level-set. The corresponding solid or double variant representation is expressed as

$$f^2(x,y,z) \leq t^2 \quad \text{(Eq.2)}$$

in which the interval [-t, t] governs the density bounds for the solid phase, which is determined by the space between the two manifolds of the network phase defined for -t < f > t. In this study, lattices composed of the strut-based Body Centred Cubic (BCC) unit cells and the surface-based Schwarz-P (SP) and Gyroid (GY) unit cells, are investigated. The equations for the latter two TPMS cells are as follows

$$f_{SP}(x,y,z) = \cos(\lambda_x x) + \cos(\lambda_y y) + \cos(\lambda_z z) \quad \text{(Eq.3)}$$

$$f_{GY}(x,y,z) = \cos(\lambda_x x) * \sin(\lambda_y y) + \cos(\lambda_y y) * \sin(\lambda_z z) + \cos(\lambda_z z) * \sin(\lambda_x x) \quad \text{(Eq.4)}$$

, where $\lambda_i = 2\pi * n_i/L_i$ governs the periodicity in three dimensions with n_i corresponding to the number of cell tessellations/repetitions along the lattice edge length L_i.

2.1.1 Density grading

Grading of the unit cell density is conducted as in [36], where *t* controls variation of the volume fraction within 3D-space such that the condition

$$f^n(x,y,z) \leq t^n(x,y,z) \qquad n = \begin{cases} 1, single\ variant\ (network\ phase) \\ 2, double\ variant\ (matrix\ phase) \end{cases} \quad \text{(Eq.5)}$$

is fulfilled. The abovementioned approach is conceptionally equivalent for the strut-based counterparts, however, the actual implementation for generating those is relying on a database of multiple unit cells with different uniform density gradients. In this study both SP and BCC lattices were linearly graded between two parallel surfaces (see Fig. 2) i.e. each lattice is defined by this maximum ρ_{max} and minimum ρ_{min} local density.

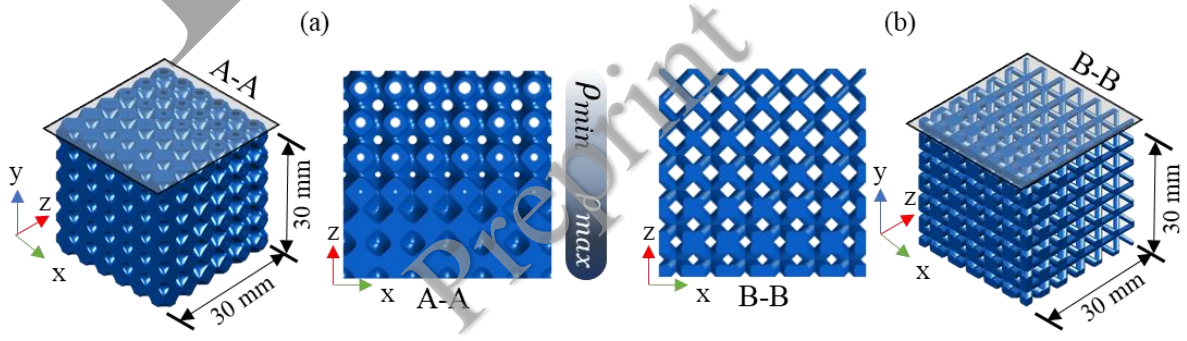

Fig. 2: Isometric and front view of a (a) SP and (b) BCC lattice with a linear density gradient in the z-direction.

2.1.2 Unit cell size grading

Structures with graded unit cell size i.e. a hybridization of unit cells of different edge lengths have been generated based on the algorithm proposed in [58], using a sigmoid function with a constant transition width across all specimens, ensuring a smooth morphing/merging between dissimilar cell counts. For this purpose the edge length of the GY and SP lattices were divided into three segments of 10mm each, constituting the design space for a set unit cell size (see Fig. 3). The severity of grading is hereby defined by the increase in the number of unit cells from one segment to another. Hence, the expression for the gradient 3-6-9 for the lattices shown in Fig. 3. It is of note that the average density between layers of different unit cell size is kept constant.

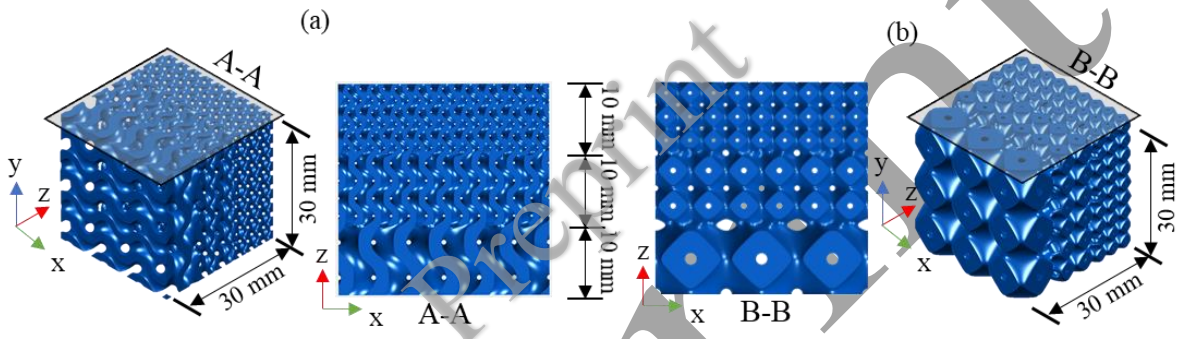

Fig. 3: Isometric and front view of a (a) GY and (b) SP lattice with a unit cell size gradient in the z-direction, realized through a cell size hybridization at two equidistant positions along the edge length. The unit cell count per edge length in the three segments changes from 3 to 6 to 9, hence the nomenclature convention 3-6-9.

2.2 Design of experiments

2.2.1 Test case matrix

Initially, a set of ungraded SP and BCC lattices with average densities of 0.2, 0.35, 0.5, 0.65 and 0.8 were printed and tested parallel and transverse to the build-direction (defined as *z*-direction for the remainder of the work). This established baseline values to classify the performance of the density graded counterparts. Fig. 4 displays the coupons printed for investigations into the density and cell size grading.

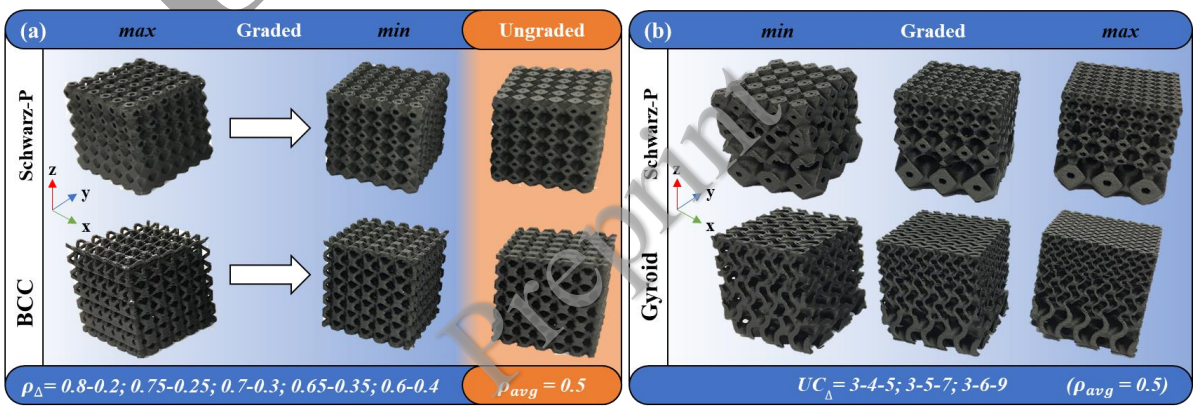

Fig. 4: Fabricated lattice specimens with unit cell (a) density grading and (b) cell size grading.

Building up from the author's previous work [64], Table 1 summarizes the entire test case matrix of this work. Five different severities of density grading (ρ_Δ) with the same relative density (i.e. average density ρ_{avg}) as the ungraded counterpart were chosen, printed in both z- and x-direction (parallel and transverse to the build direction) to investigate the effect of printing direction on the mechanical performance. On the other hand, three different unit cell size gradients (UC_Δ) were investigated for the SP and GY lattices while keeping $\rho_{avg} = 0.5$. In all test cases, the loading direction aligns with the direction of the gradient.

Table 1: Test case matrix summarizing the number of specimens tested for each configuration with respect to the average density ρ_{avg}, the density and unit cell size gradient (ρ_Δ and UC_Δ) as well as the test direction.

		Ungraded					**Graded**							
		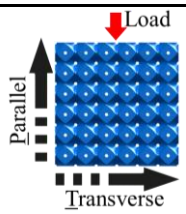					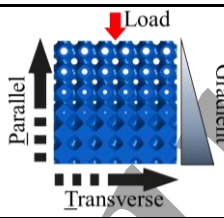					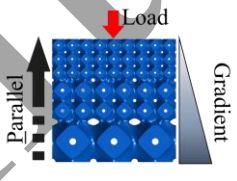		
Avg. density: ρ_{avg}		0.2	0.35	0.5	0.65	0.8			0.5				0.5	
Gradient: ρ_Δ & UC_Δ		n.a.					0.6 - 0.4	0.6 - 0.35	0.7 - 0.3	0.7 - 0.25	0.8 - 0.2	3-4-5	3-5-7	3-6-9
No. of tests	**P**	2	2	2	2	2	2	2	2	2	2	2	2	2
	T	2	2	2	2	2	2	2	2	2	2	/	/	/

Note: "P" and "T" refer to the number of tests conducted parallel and transverse to the build direction.

2.2.2 Manufacturing and quasi-static experimental testing

The specimens were printed with the *Markforged Inc. MarkTwo* fused deposition modelling (FDM) machine, using short carbon fibre-reinforced nylon (material properties as obtained from the manufacturer [65]). The stl. files were sliced using the *Markforged's Eiger* software, whereby the specimens were intended to be self-supported. Two roof-/floor- and wall-layers were selected, and the remaining volume was printed with a ±45° infill.

As the lattices are modelled in a voxel environment, there is always a small error between the target and numerically achievable value for the density. The subsequent slicing of the model i.e. the transformation into a gcode that defines - among others - the infill pattern, can lead to further deviations. This is the case with most slicers, as the bead width is not changed in-situ, using an adaptive extrusion value to accommodate for passages that do not match a multiple of the bead width. Finally, the layer-by-layer extrusion process is naturally associated with producing inter-bead pores causing a discrepancy from design-to-print. The subsequent results were therefore normalized using the actual mass of the printed specimens and the material's density. If not otherwise specified, the term "density" refers to the theoretical value in the remainder of this work.

It is important to note that the cubic shape of the specimens prevents a true uniaxial stress state. In order to provide further insight into the deformation behaviour of the FGLs, recordings with an optical strain gauge were made for which a speckled pattern with a dot size of approximately 0.5mm was applied on the surfaces of the specimens. Individual strain measurements in the density graded specimens were taken at the centre of the front-facing cubic specimens and 2D strain maps were used to showcase the overall distribution in the cell size graded lattices. Another important issue to mention is the edge effect in cellular solids stemming from the unit cell count per edge length. Previous studies [66,67] have conducted convergence studies on cubic TPMS lattices, determining the number of unit cells required per edge length such that the upper bound for e.g. the modulus is matched. The error for a 3x3x3 and a 4x4x4 lattice was found to be in the realm of 1% and 0.2%, respectively [66,67], substantiating negligible influence even for the cell size graded lattices in this study, composed of 9 unit cells in the bottom layer.

2.3 Assessment of moduli and energy absorption capability

The elastic modulus of the five ungraded lattices of dissimilar density was determined from the initial linear slope in the nominal stress-strain curve i.e. the stress was calculated from the load on the nominal surface area of the lattice (see Fig. 5). If not expressly specified, the remainder of this work will report on nominal values i.e. capture the global lattice response and average properties, neglecting the local material behaviour. Furthermore, it is of note, that the stress and strain distribution varies due to the shape of the specimen and the free edges.

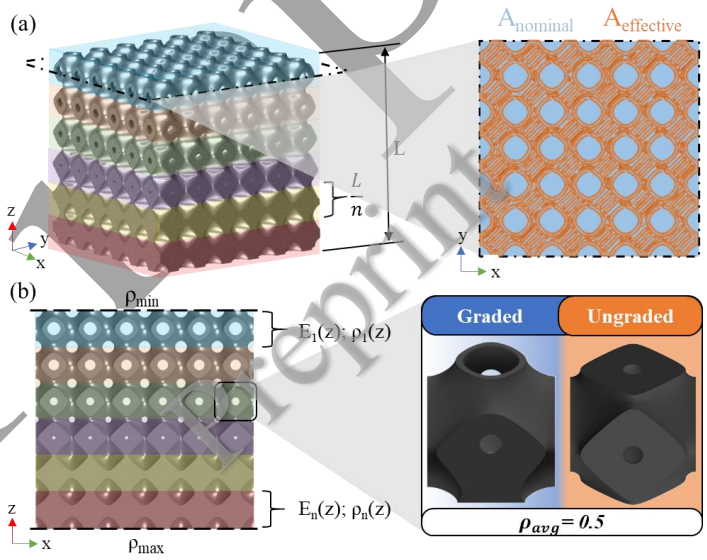

Fig. 5: Schematics of a linearly graded cubic SP lattice of edge length L composed of n different unit cell regions of different average density. (a) Isometric and cross-section view, highlighting the nominal (global) vs the effective (local) surface area. (b) Frontal view with a close-up of graded and ungraded single unit cells of identical density, illustrating the continuity of the density gradient throughout individual unit cell regions.

On the basis of the nominal moduli E^{nom} of the ungraded lattices, the standard scaling law (see Eq.6), as described by Gibson and Ashby [68], was employed to relate the

experimentally determined relative moduli E_{rel}^{nom} (nominal moduli E^{nom}normalized by the bulk modulus of the material E_S) to the relative lattice density ρ_{rel}. From this data of the baseline lattices, the performance of the graded equivalent was derived. As the relative density changes continuously along the z-direction in the graded lattices, every single one of the *n* unit cell regions has a different average unit cell density and hence a disparate modulus, as illustrated in Fig. 5. The curve fit for relative modulus can thus be expressed as

$$E_{rel}^{nom}(z) = C_1(\rho(z)_{rel})^m \quad \text{(Eq.6)}$$

with C_1 representing a constant governing the geometrical features and taking a typical value between 0.1-4.0, whereas the exponent *m* lies around 2 [68]. As the relative properties are considered, the stiffness is zero for $\rho_{rel} = 0$ and maximal for $\rho_{rel} = 1$, i.e. equal to the bulk modulus E_S. Hence, these bounds have been considered in fitting the experimental data. With the change in density $\Delta\rho_{rel}$, defined as absolute difference between the maximum ρ_{rel}^{max} and the minimum ρ_{rel}^{min} density at the two parallel surfaces (see Fig. 5), the density can be expressed as a function of *z*

$$\rho(z)_{rel} = \rho_{rel}^{min} + \frac{\Delta\rho_{rel}(L-z)}{L} \quad \text{(Eq.7)}$$

where *L* is the total edge length of the specimen. On this basis, the total nominal stiffness of the density graded lattices was determined through integration along the gradient as proposed in [41]:

$$\frac{1}{E_{tot}^{nom}} = \frac{1}{L}\int_0^L \frac{1}{E_{rel}^{eff}(z)}dz \quad \text{(Eq.8)}$$

As the average cross-section area between the individual unit cell regions of the ungraded lattice is equal, the nominal stress-strain curves functioned as the basis for the determination of the energy absorption per unit volume. However, due to the continuous change of the cross-section in the graded counterparts, the stress distribution is no longer uniform. Therefore, it is only adequate to plot the load-displacement curves from which the absorbed energy is directly computed.

As the fibre volume fraction of the filament used for printing is relatively small (~9%), the Halpin-Tsai model [69] was used to predict the potential for this type of FGLs assuming the theoretically highest achievable fibre volume fraction for FDM processes, which is estimated to be around 40% [70]. The model for predicting the Young's modulus of the composite is

$$\frac{E_c}{E_m} = \frac{1+\eta\xi\varphi_f}{1-\eta\varphi_f} \qquad \text{with: } \begin{cases} \eta = (\frac{E_f}{E_m} - 1)/(\frac{E_f}{E_m} - \xi) \\ \xi = 2\frac{l}{d} \end{cases} \quad \text{(Eq.9)}$$

where the ratio between the modulus of the composite E_c and the matrix E_m is determined from the fibre volume fraction φ_f, the modulus of the fibre E_f as well as the length *l* and diameter *d* of the fibre.

Investigations into the energy absorption capability generally employ nominal stress-strain data (if not otherwise specified) and utilize the densification onset strain ε_{DO} as a

reference value, describing the point after which the slope of the load-displacement is rapidly approaching the one of the initial linear-elastic regions, as the cell walls start to coalesce, until the densification strain ε_D is reached. This strain is determined using the energy efficiency method [71], whereby the efficiency κ can be defined as

$$\kappa(\varepsilon) = \frac{1}{\sigma(\varepsilon)} \int_0^{\varepsilon} \sigma(\varepsilon) d\varepsilon \quad \text{i.e.} \quad \kappa(u) = \frac{1}{P(u)} \int_0^{u} P(u) du \qquad \text{(Eq.10)}$$

as derived from either the stress-strain (σ-ε) or load-displacement (P-u) curves, respectively. ε_{DO} is subsequently determined at the plateau i.e.

$$\frac{d\kappa(\varepsilon)}{d\varepsilon} = 0 \quad \text{i.e.} \quad \frac{d\kappa(u)}{du} = 0 \qquad \text{(Eq.11)}$$

3 Results

3.1 Ungraded baseline lattices: Physical properties and mechanical performance

Fig. 6 illustrates the nominal stress-strain curves, indicating generally higher compressive moduli of the stretching-dominated SP lattices than the bending-dominated BCC lattices. This is independent of ρ_{avg}, which is in line with earlier findings [72], and the build direction. However, the high-density BCC lattices tested transverse to the build direction, display a greater dispersion compared to the ones tested parallel to the build direction.

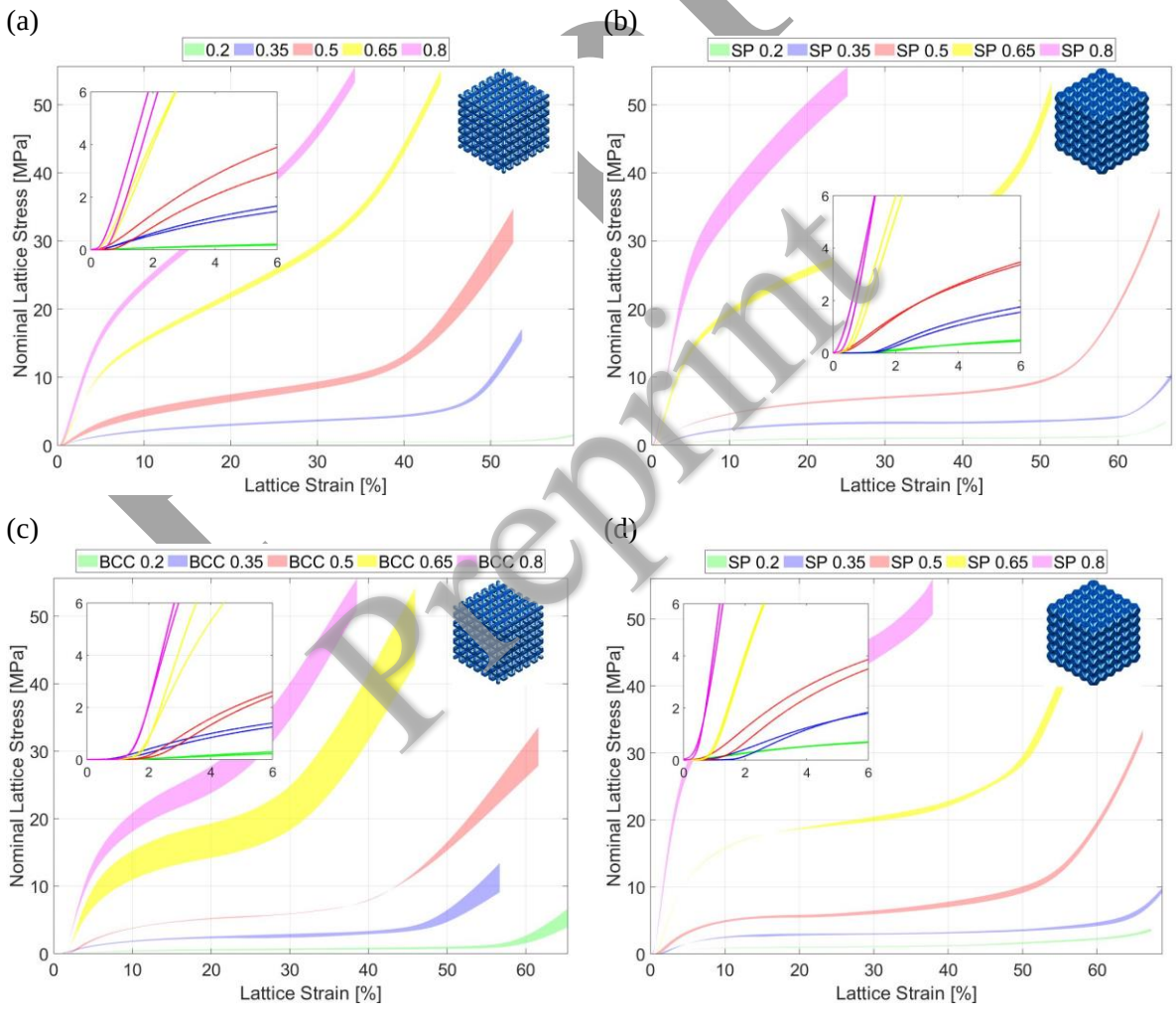

Fig. 6: Nominal stress-strain curves of the uniform (a)/(c) BCC and (b)/(d) SP lattices of different density, tested (a)/(b) parallel and (c)/(d) transverse to the build direction.

As a summary, Fig. 7 highlights two key parameters for the ungraded lattices: 1) the relation between the theoretical and actual lattice density and 2) the nominal compressive modulus of the ungraded lattices with respect to cell type, average lattice density and build direction. It was found that the numerical density values are in close agreement with the targeted (i.e. theoretical) values, whereas the actual density is systematically lower than anticipated, owing to the pores created during printing (see Fig. 7a). The experimental density value was hereby determined by means of the print material density of 1.2 g/cm^3 [73] and the measured specimen mass. Likewise, the overall relative density of the graded BCC and SP lattices was calculated and came to 0.42 ± 0.005 and 0.43 ± 0.013, respectively.

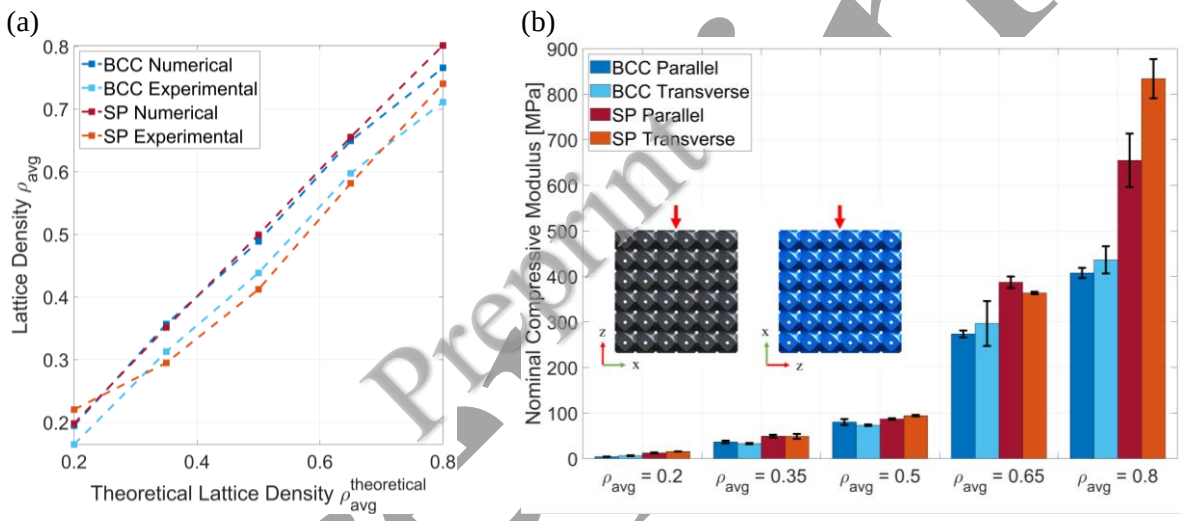

Fig. 7: (a) Relation between the theoretical, numerical and actual (i.e. experimentally determined) lattice density of the ungraded lattices. (b) Nominal compressive Young's moduli of the ungraded BCC and SP lattices as a function of the theoretical volume fraction and build direction (z-axis) including error bars capturing the standard deviation.

Fig. 7(b) highlights the nominal compressive modulus of the ungraded lattices with respect to cell type, average lattice density and build direction. Generally, at low ρ_{avg} up to 0.5, there is only little improvements in stiffness, however, notable increases were observed from $\rho_{avg} = 0.5$ to $\rho_{avg} = 0.65$. This growth is bigger for the SP lattice which can most likely be attributed to the transition from open to closed unit cells, whereby the share of cell wall stretching to bending increases in favour of the former, providing greater axial cell wall stiffness [68]. With increasing cell wall thickness from $\rho_{avg} = 0.65$ to $\rho_{avg} = 0.8$ this effect is reinforced.

Similarly, it was observed that the for a low average density up to $\rho_{avg} = 0.5$, the differences between the building directions were marginal and not coherent, however, the BCC lattices displayed a slightly higher stiffness for specimens of $\rho_{avg} = 0.65$ and $\rho_{avg} = 0.8$, tested transverse to the build direction. However, the most significant difference was observed in the

SP specimens with the highest average density. Generally layered structured can be considered transversely isotropic and with the introduction of fibres the difference between in-plane and out-of-plane properties becomes even greater. In FDM processes high aspect-ratio short fibres are always aligned with the print/track direction due to the shear force in the nozzle [15,21]. Micrographs presented in [74–76], confirm that this is also the case for the short-fibre reinforced polymer under investigation (aspect ratio ~14:1), using a nozzle with an internal diameter of ~0.36mm. For specimens tested transverse to the build direction, an increasing lattice density ρ_{avg} results in a larger percentage of fibres and print tracks being aligned with the load-direction (segment length and continuity together with consistent double wall layer) and more effective design space becomes occupied by the ± 45° infill (see Fig. 8). Analogously to the behaviour described through the standard laminate composite theory - to which 3D printed specimens conform well [77,78] - it is assumed, that this is the reason for the better performing high-density SP lattice tested transverse to the build direction.

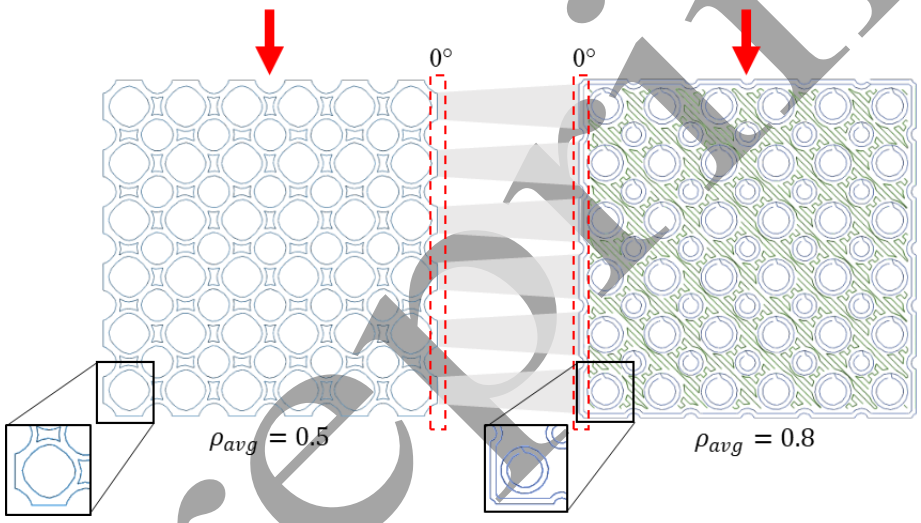

Fig. 8: Comparison of print slices of uniform SP lattices with different average density taken at identical positions (hight of specimen). High density lattices illustrate a greater percentage of 0° paths (aligned with load direction) and ± 45° infills.

3.2 Graded lattices

3.2.1 Lattices with graded unit cell density

Fig. 9 illustrates the individual deformation stages of the graded SP and BCC lattices up to 60% nominal strain, at which the specimens take up a trapezoidal shape. In comparison, the ungraded counterpart displays no such tilt of the edges at this strain. As the Poisson's ratio is independent of the unit cell relative density the tilt in the graded lattices is due to the dissimilar stiffness of the individual unit cell layers.

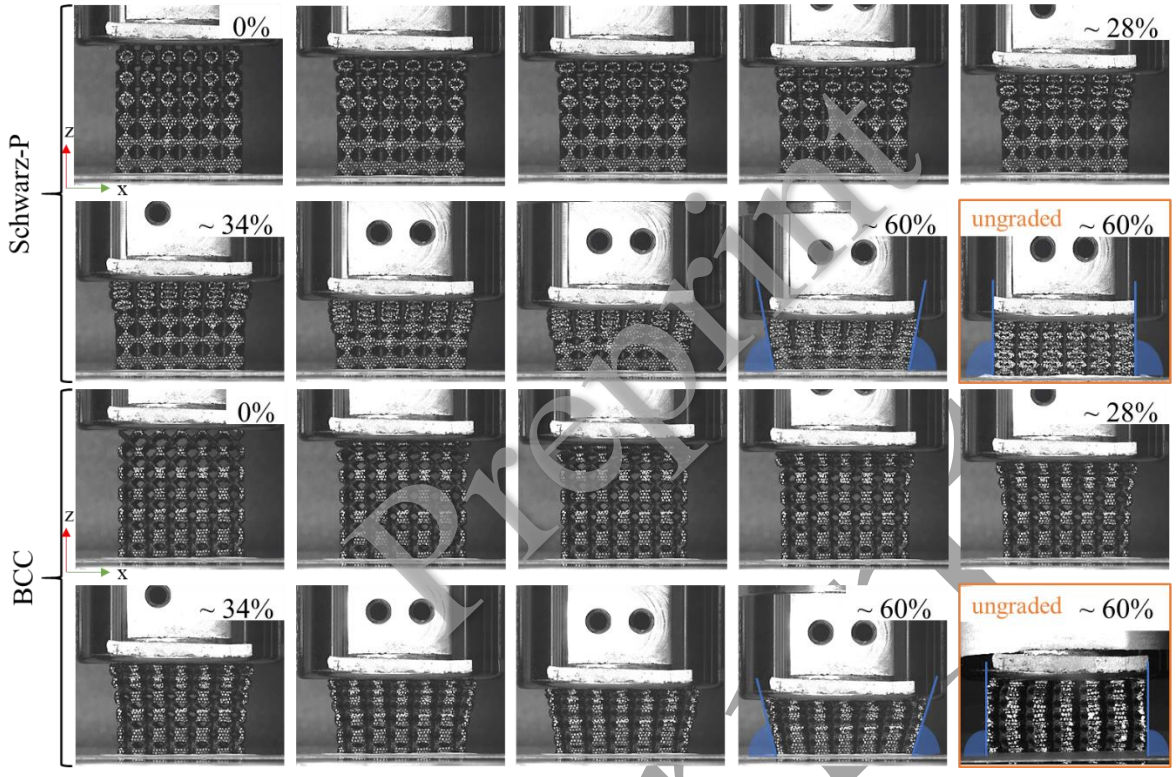

Fig. 9: Deformation stages of the most severely graded (0.8-0.2) BCC and SP lattices during compression for different nominal lattice strains up to 60%. Each final two images highlight the trapezoidal shape of the graded vs the unchanged shape of the uniform counterpart.

The associated load-displacement curves of the graded lattices are displayed in Fig. 10, displaying distinct load-drops and plateaus for the most severe density gradients between the linear elastic and the plateau region. These represent the failure of lowest-density unit cell layers before transitioning into plateau strain region, which is only really pronounced for the ungraded SP lattice, whereas the remaining specimens illustrate a positive plateau strain rate. It is noteworthy that the SP lattices tested parallel to the build direction show a distinct point of intersection at around 10 mm displacement before which the most severely graded lattices take lower loads for a given displacement than the ungraded counterpart and after which this state is reversed. The SP lattices tested transverse to the build direction display a similar trend, without having such a unique point of inversion. The ungraded BCC lattice tested parallel to the build direction outperformed the graded counterparts and vice versa for the specimens tested transverse to the build direction. Generally, the load-displacement curves of identical specimen types are very tight showing great consistency, only the specimens tested transverse to the build direction displayed greater variability at large deformation. These findings provide a good guide as to the usefulness of grading with respect to cell type, loading direction and envisaged deformation range and can, therefore, lend itself to infer improved AM-designs.

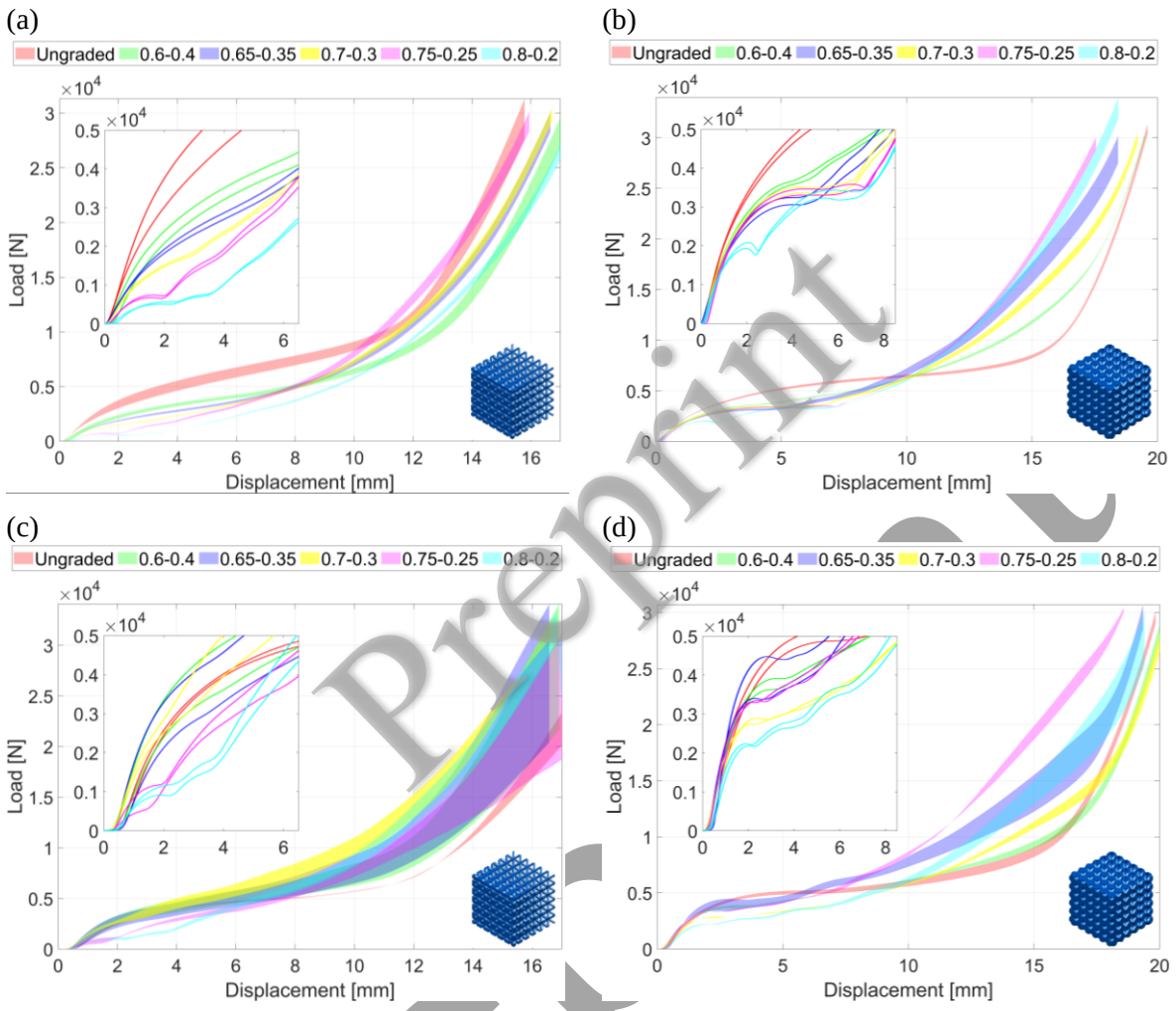

Fig. 10: Load-displacement curves for the graded (a)/(c) BCC and (b)/(d) SP lattices compared to the ungraded equivalents with equal mass tested (a)/(b) parallel and (c)/(d) transverse to the build direction.

The following cumulative energy absorption (see Fig. 11), derived from the load-displacement curves, visualize the concrete performance of the lattices for a given lattice strain. Except the BCC lattices tested parallel to the build direction, the ungraded lattice underperforms for greater lattice strain. The gradual increase in resistance in the graded lattices enforces a greater displacement that needs to be covered before the lattices have the same effective stiffness as their ungraded equivalent and could hence lend themselfs greatly for applications considering impacts.

The SP lattices displayed a much tighter set of curves, particularly for the specimens tested parallel to the build direction, as compared to the BCC lattices. Grading was found to have a more detrimental effect on the energy absorption capability of the BCC than for the SP counterparts. The most severely graded SP lattice was found to outperform the BCC equivalent throughout, and similarly, the graded SP lattices were found to generally absorb more energy up to the densification onset of the respective ungraded lattice than the graded BCC counterparts. However, the latter surpass the cumulative energy absorption capability of the surface-based lattices beyond this strain.

Considering the cumulative energy absorption results for the tests conducted transverse to the build direction, it becomes apparent, that the BCC lattices perform slightly better than in parallel direction, whereas no significant difference was observed in the SP lattices.

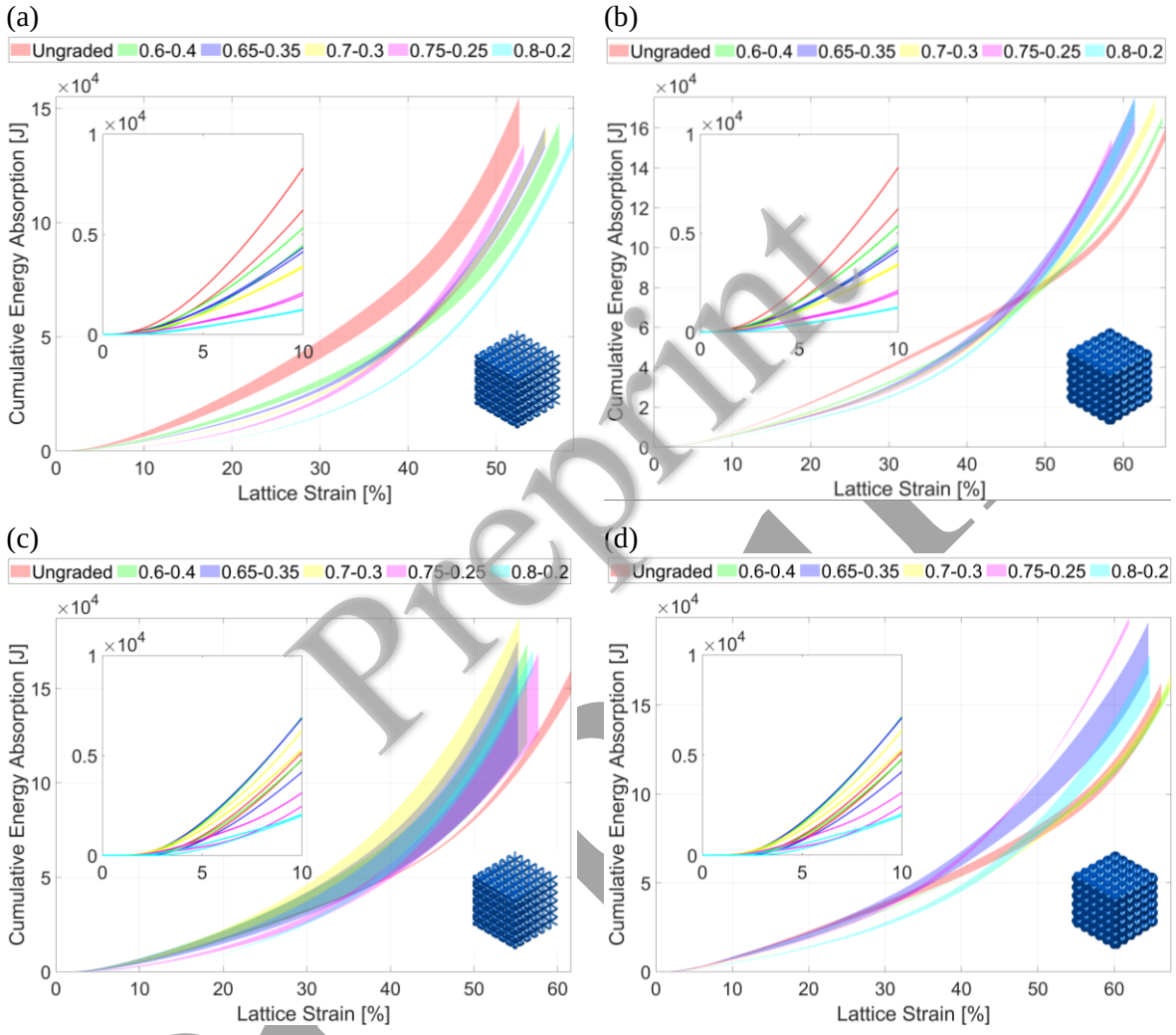

Fig. 11: Cumulative energy absorption curves for the ungraded and graded (a)/(c) BCC and (b)/(d) SP lattices of equal relative density tested (a)/(b) parallel and (c)/(d) transverse to the build direction.

The coherent intersection points between the graded SP specimens tested parallel with the ungraded counterpart (see Fig. 10 & Fig. 11) reveal a superior energy absorption capability of graded lattices compared to the ungraded counterpart for large deformations i.e. lattice strains above 50%. The average break-even strain ε_{BE} i.e. intersection point for the graded lattices with the ungraded lattice (see Table 2), with regard to the cumulative energy absorption, lies within the realm of the densification onset strain ε_{DO} of the uniform lattice (49.3% ± 2.3) as shown in Table 2.

Table 2: Break-even strain ε_{BE} for the cumulative energy absorption between the graded and ungraded lattice with dissimilar density gradient ρ_{Δ}.

$\boldsymbol{\rho_{\Delta}}$	0.6-0.4	0.65-0.35	0.7-0.3	0.75-0.25	0.8-0.2
$\boldsymbol{\varepsilon_{BE}}$ **[%]**	51.3 ± 2.4	46.1 ± 2.3	49.3 ± 1.7	46.4 ± 1.1	48.6 ± 1.1

3.2.2 Lattices with graded unit cell size

Fig. 12 displays the load-displacement and the deduced cumulative energy absorption curves for the SP and GY lattices with three different severities of unit cell size grading. Generally, the SP lattices showcase less dispersion both between the individual tests and the different cell size configurations compared to the GY lattices. Moreover, the former displays a lower strain rate in the plastic plateau region with a sharp increase in load at densification, as opposed to the GY lattices which illustrate a higher strain rate after the linear-elastic region with a less distinct load increase beyond 15mm displacement.

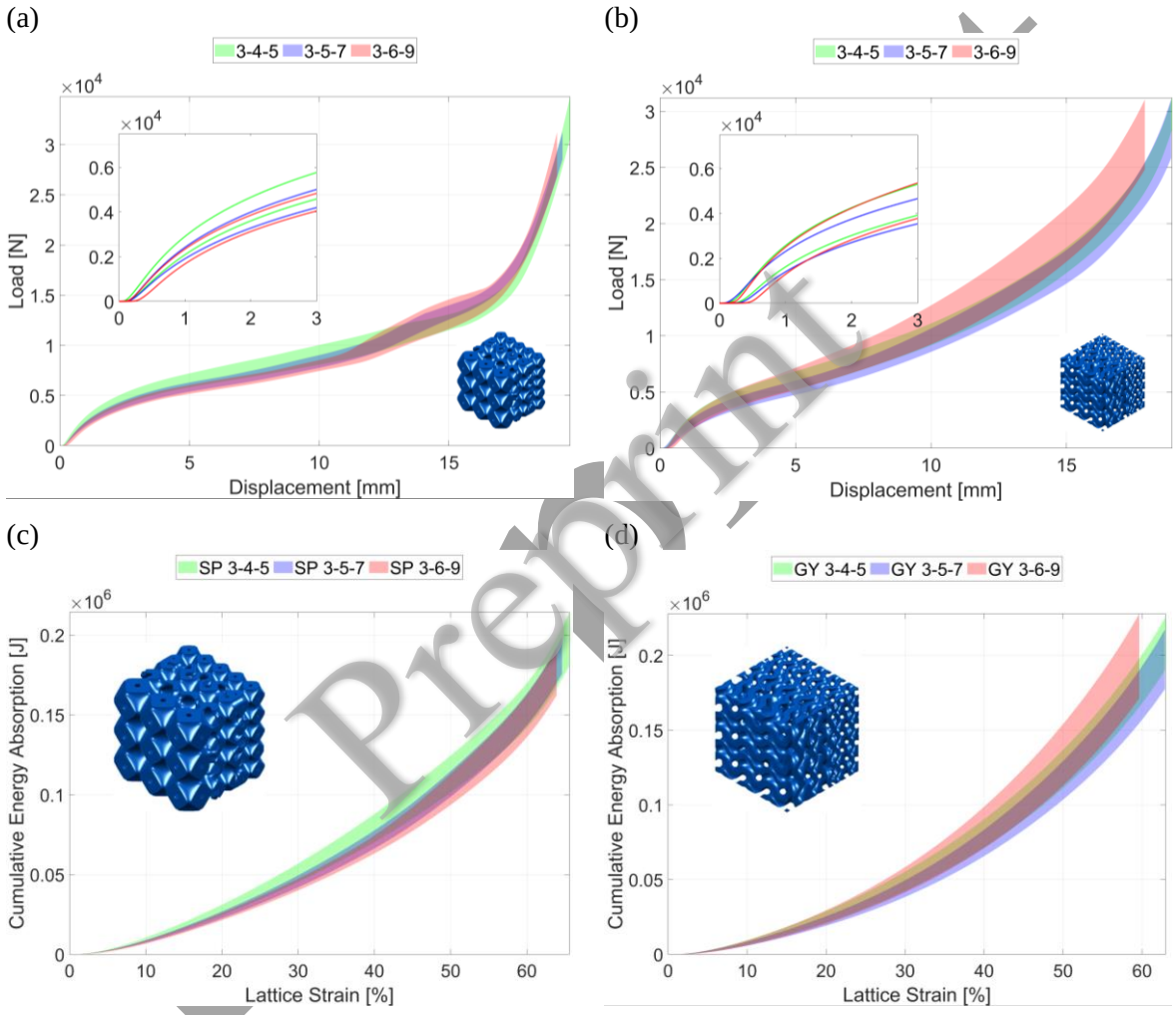

Fig. 12: (a)/(b) Load-displacement and (c)/(d) cumulative energy absorption curves of unit cell graded (a)/(c) SP and (b)/(d) GY lattices.

The average Young's moduli, as determined from the linear-elastic region in the corresponding nominal stress strain curve are displayed in Fig. 13. Apart from generally higher moduli in the GY lattices compared to the SP lattices, no clear trend can be derived from these values. However, due to the constant relative density through the thickness of these specimens a significant influence of the severity of unit cell size grading on the Young's modulus is not to be expected, as proven by Gibson and Ashby's scaling law [68]. Reasons for variability could possibly stem from manufacturing (e.g. wall thickness influences infill) and the change

in the morphology of the hybridized zones, but further investigations are required to shed light on those influencing parameters.

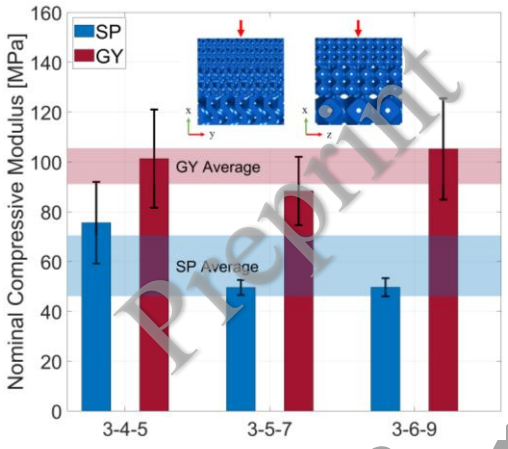

Fig. 13: Average nominal Young's moduli for the unit cell size graded SP and GY lattices, including individual standard deviation and overall unit cell type average as indicated by the horizontal bands.

The average densification onset ε_{DO} strain was found to be 54.4% ± 0.6 for the SP lattice and 55.7% ± 1.0 for the GY lattice, respectively. Moreover, the SP lattices displayed a more severe load increase and a minor rise in the most severely graded lattice prior to ε_{DO}, indicating an intermediate densification of some sort. Generally, the SP lattices displayed lower variability in the plastic-densification region compared to the GY lattices but overall, the performances are comparable.

In Fig. 14 the 2D axial (ε_z) and transverse (ε_y) strain maps are illustrated for 10% and 30% lattice strain to better identify the differences in the structural behaviour. For both the SP and GY lattices, the strain distributions are homogeneous across the front surface of the specimen in both direction for a lattice strain of 10%, indicating a more evenly distributed load. However, thin sections of lower axial strain were identified around the hybridized sections and/or the topmost layer of the most severely graded lattices. These sections become more pronounced at 30% strain while the GY lattices demonstrate a strain gradient towards the bottom layer (greatest unit cell size) for low and intermediately graded lattices. The most severely graded specimen however, shows an interruption in the middle region (intermediate unit cell size with lower strain values). The latter suggests that the local stiffness is higher for the cell size corresponding to 6x6 unit cell segment as opposed to 3x3 and 9x9, however, the transverse strain highlights the opposite effect i.e. higher strains in the middle sections. Hence, the lack of unit cell symmetry in GY can result in a change in parallel and transverse stiffness dependent on the unit cell size. This needs further investigations as this suggests that there is not a gradual convergence towards a stiffness value that is independent of the edge effect and therefore requires attention when selecting cell size and type. On the basis of the deformed shapes, the unit cell size graded SP lattices demonstrate the same trapezoidal-like shape as the density graded specimens, whereas the GY lattices retain their shape similar to the ungraded lattices.

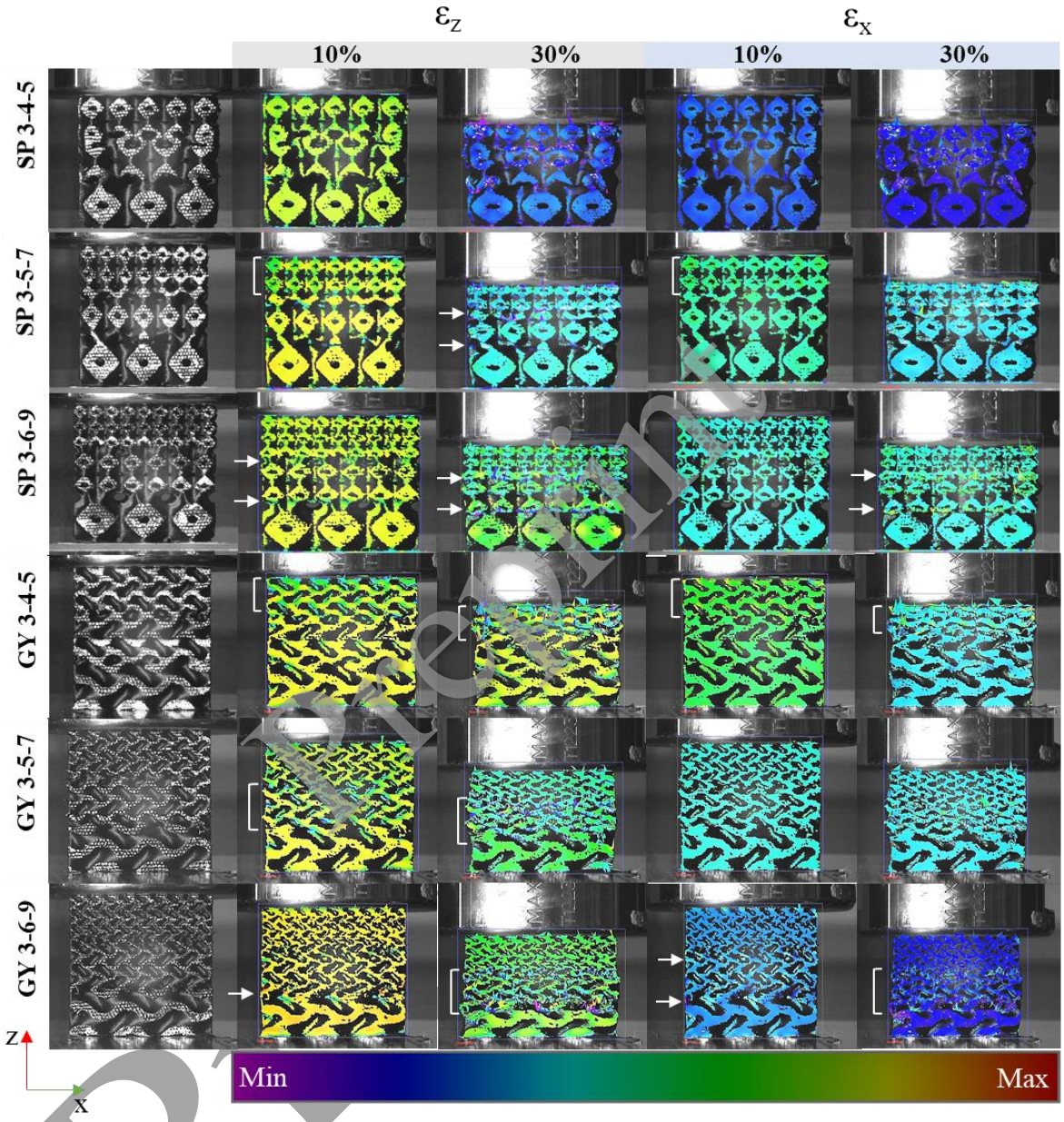

Fig. 14: 2D strain maps in z- and x-direction at 10% and 30% lattice strain for the SP and GY unit cells with different severities of unit cell size grading. White arrows and brackets highlight the extremes.

4 Discussion

4.1 Ungraded baseline lattices: Densification onset and energy absorption

As shown in Table 3, the densification onset strain ε_{DO} could only be determined up to $\rho_{avg} = 0.5$ and $\rho_{avg} = 0.65$ for the BCC and SP specimens, respectively. Lattices with a higher average density have led to a convergence of the energy efficiency curve without providing a distinct optimum. This implies, that the cell wall interactions are muted at high volume fraction, resulting in a smooth transition into actual material densification. The BCC lattices showcased a drop in ε_{DO} with increasing ρ_{avg} for both sets of specimens, whereas no such trend can be derived from the SP lattices, which demonstrate a fairly constant ε_{DO}. Table

3 also displays the corresponding cumulative energy absorption up to the densification strain $w_{\varepsilon_{DO}}$. It was observed, that a rise in average lattice density results in increased energy absorption and that the transverse build direction results in a lower absorption capability except for the BCC specimen at $\rho_{avg} = 0.2$. A significant increase i.e. a multiplication of the cumulative energy absorption by a factor of 2-3 was observed from $\rho_{avg} = 0.5$ to $\rho_{avg} = 0.65$ in the SP specimens. Overall, SP specimens outperform BCC counterparts independent of ρ_{avg} and build direction.

Table 3: Densification onset strain ε_{DO} and cumulative energy absorption up to the densification onset $W_{\varepsilon_{DO}}$ for BCC and SP lattices tested parallel and transverse to the build direction

	BCC				**SP**			
	$\boldsymbol{\varepsilon_{DO}}$	$\boldsymbol{W_{\varepsilon_{DO}}}$	$\boldsymbol{\varepsilon_{DO}}$	$\boldsymbol{W_{\varepsilon_{DO}}}$	$\boldsymbol{\varepsilon_{DO}}$	$\boldsymbol{W_{\varepsilon_{DO}}}$	$\boldsymbol{\varepsilon_{DO}}$	$\boldsymbol{W_{\varepsilon_{DO}}}$
Build direction	*Parallel*		*Transverse*		*Parallel*		*Transverse*	
$\boldsymbol{\rho_{avg}}$ **= 0.2**	51±0.2	977±64	52±64	1531±64	58±64	2546±64	46±64	2236±64
$\boldsymbol{\rho_{avg}}$ **= 0.35**	42±0.1	3429±64	44±64	2744±64	59±64	4961±64	57±64	4607±64
$\boldsymbol{\rho_{avg}}$ **= 0.5**	38±0.2	4979±64	39±64	3597±64	49±64	5967±64	49±64	5597±64
$\boldsymbol{\rho_{avg}}$ **= 0.65**	n.a.	n.a.	n.a.	n.a.	45±64	17153±64	48±64	13387±64
$\boldsymbol{\rho_{avg}}$ **= 0.8**	n.a.	n.a.	n.a.	n.a.	n.a.	n.a.	n.a.	n.a.

4.2 Graded lattices

4.2.1 Failure and structural response

As a nominal stress-strain curve would not accurately represent the individual stresses in each unit cell layer of the graded lattice, Fig. 15 illustrates the local unit cell strain for the BCC and SP lattice graded from 0.8-0.2. The initial displacement-range up to ~0.5-1mm (linear-elastic region up to the onset of lattice yielding i.e. load plateau), reveals a highly different strain distribution in the z-direction (i.e. loading direction) with the BCC specimen taking a concave shape whereas the SP specimen displays a convex distribution. It is of note, that the increase in strain at the unit cell layer with the highest density (i.e. between 25 and 30mm) are relicts caused by measurement inaccuracies. Hence, when the strain has already gone to zero in layers of lower density it can be ignored for these unit cell regions. At displacements up to around ~3.5mm, the vertical lattice strains in the BCC specimens go to zero earlier than in the SP specimen, implying a less uniform load distribution in the bending dominated unit cell lattice. This more sequential collapse in the BCC lattice, as indicated by the higher overall unit cell strain values in the first third of the lattice (0-10mm), explains the lower stiffness compared to the SP lattice. At displacements above ~4mm, the distributions between the two lattices correspond better. The transverse unit cell strains up to ~3.5mm showcase a similar trend as the parallel ones and match well with the observations of the deformation stages shown in Fig. 9.

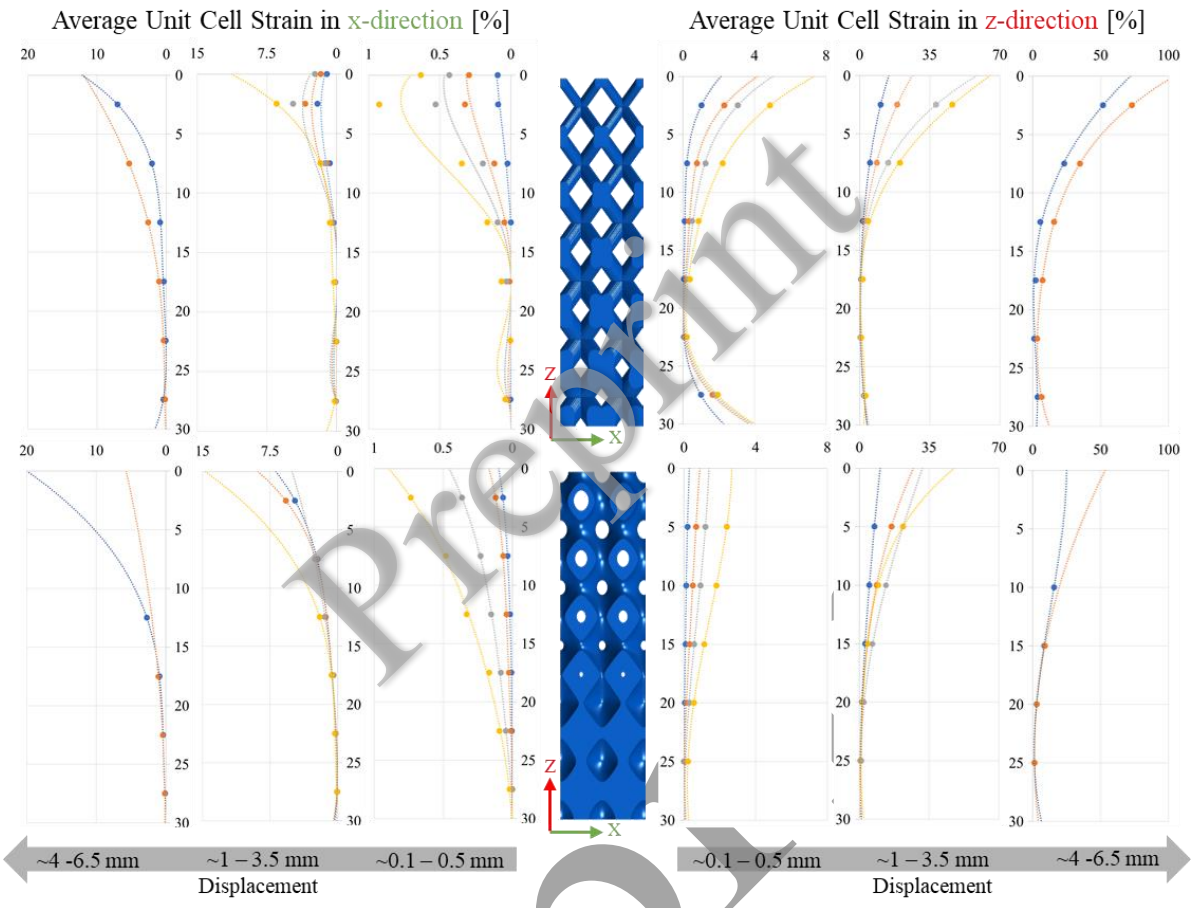

Fig. 15: Representation of the average unit cell strain distribution for different displacement ranges fitted with an n-1 order polynomial for n data points. Displayed are both the strain in x- and z-direction for the BCC and SP specimen with a relative density gradient from 0.8-0.2 measured in the centre of the specimen surface.

Some deformed specimens are illustrated in Fig. 16, exemplifying the crack formation with respect to cell type and build direction. It was found that the SP specimens tested parallel to the build direction have shown hardly any signs of cracks, whereas, the corresponding BCC lattices displayed horizontal cracks along the unit cell interfaces. This can be explained by x-shaped struts acting like a hinge when loaded and hence promoting tensile stress concentrations at the corners, where the geometry changes abruptly. With the interlaminar strength being lower than the in-plane strength in layered composites fabricated with FDM, commonly due to the inter-bead porosity and other manufacturing-related issues such as wetting, cracks are likely to develop along the build plane as observed in the test specimens. Another factor - frequently observed in composites - is crack-steering through the fibres i.e. cracks can easily propagate in fibre direction rather than having to circumvent them. However, it is important to note, that these are assumptions for the cause of the crack formation, requiring further investigations for absolute conclusiveness.

Similarly, vertical cracks were observed in the BCC lattices tested transverse to the build direction (i.e. along the build plane). As the BCC lattices are bending dominated the minimum fibre length gains importance, especially in conjunction with the ductile nylon matrix, however, significant growth in stiffness should not be expected as the interlaminar

properties will be unaffected. The same applies to the specimens tested transverse to the build direction and thus the stiffness values are equal for a range of average lattice densities (see Fig. 7).

Despite the stretching-dominated nature of the SP specimens, the lattice will inevitably undergo local bending particularly when the cells are open. This has led to cracks beyond a lattice strain of 50%, initiated in the circular openings of the specimens tested transverse to the build direction where the material strength is only governed by the inter-plane bonding strength i.e. polymer matrix. In return, this explains that cracks fail to appear in the lattices loaded parallel to the build direction because the layers and fibres are arranged transverse to the potential crack direction and therefore need to overcome a higher crack initiation resistance.

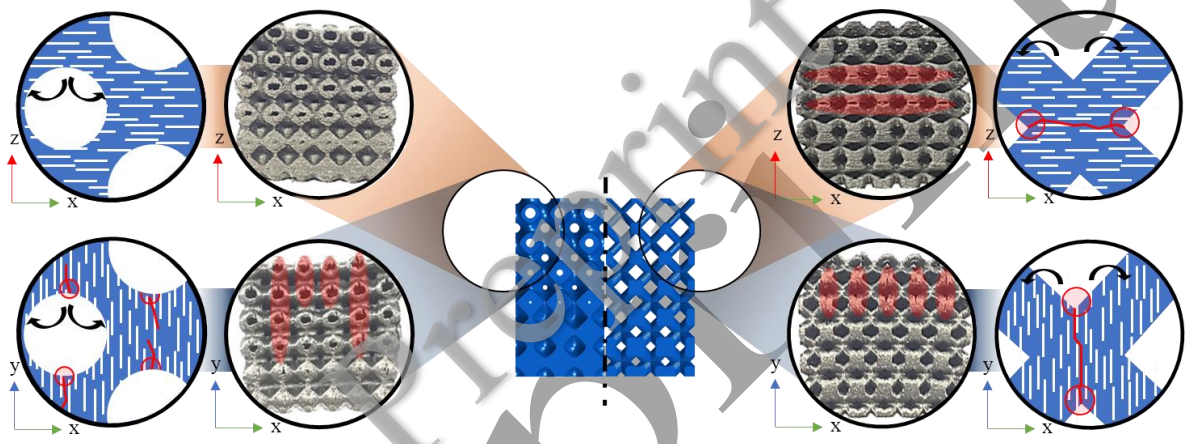

Fig. 16: Crack formation (highlighted in red) in the density graded SP (left) and BCC (right) lattices (70% to 30%) tested parallel and transverse to the building direction z, accompanied by schematic drawings.

Consequently, a greater variability, particularly for the BCC specimens, was observed in the load-displacement curves for specimens tested transverse to the build direction (see Fig. 10). Overall, this work shows smoother load-displacement curves compared to e.g. a previous study by Maskery et al. [37] in which unreinforced FGLs with a piece-wise variation of constant unit cell density ρ_{avg}, were tested. This can most likely be attributed to a true linear density gradient through the thickness (i.e. density gradient within individual unit cells), avoiding brittle and catastrophic failure.

All the SP lattices with unit cell size gradient demonstrated horizontal and vertical cracks in the front surface of the largest unit cells (see Fig. 17) and occasionally signs of small horizontal cracks in layers of intermediate unit cell size. The horizontal cracks in the GY lattices were significantly smaller and occurred exclusively in the lowest layer i.e. in the largest unit cells. The failure in the region of large unit cells is indeed in accordance with findings in [60], where authors referred to possible manufacturing-related causes such as inferior wetting in large cells [79]. This could also explain the observed cracks in the bottom layer, as individual print paths have more time to solidify before an adjacent path is being printed and thus ensure worse wettability. Furthermore, as opposed to [60], no shear band failures were observed in this work, which is most likely owed to the plasticity of the nylon specimens.

Another aspect to consider is the edge effect, which is theoretically higher in the bottom layer (i.e. lower amount of unit cells), possibly constituting a lower local stiffness. As no significantly higher or consistent difference in strain between the bottom layers and the remaining two layers was observed (see Fig. 14) for up to 30% lattice strain and in light of the marginal error expected for a 3x3x3 lattice configuration as reported in [66,67], the edge effect is assumed to be negligible. Thus, values obtained in the linear-elastic and major parts of the plastic region are only marginally - if at all - influenced by this effect. In fact, as the failure in the SP lattices occurred at high strains (> 50%) and followed the same principle as explained above for the density graded lattices, it seems plausible that a higher bending moment at the circular opening compared to the smaller unit cells, stemming from the load distribution, could be a reason for the local crack development.

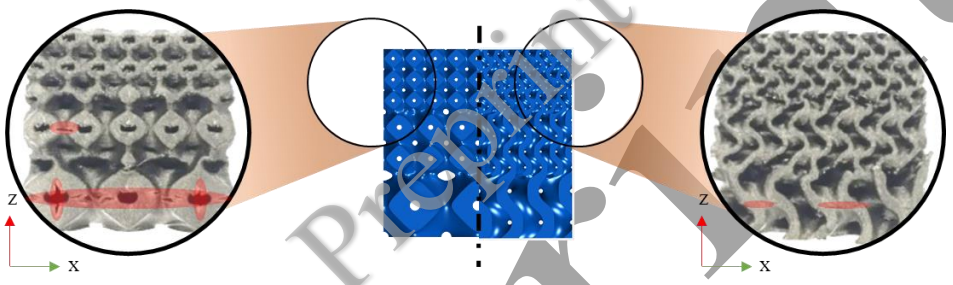

Fig. 17: Crack formation (highlighted in red) in unit cell size graded SP (left) and GY (right) lattices (3-5-7 unit cell count gradient).

It is important to mention that the fibre content in the filament is very low (~ 8%), potentially supplying insufficient overlaps and therefore compromising bending stiffness. However, based on the above findings, it is assumed that a higher fibre volume fraction will only really improve the stiffness of the SP lattices. It is therefore concluded, that the inter-plane bonding strength and the unit cell geometry are the key influencing variables for the lattice performance. It is also of note, that the fibre-reinforced nylon lattices did not experience cracks i.e. failure at the necks of the SP unit cells as found in the lattices manufactured from unreinforced nylon 12 [67]. Apart from delaminations, experienced in specimens tested transverse to the build direction, no severe failures like shear band deformations, as recently reported for density graded metal-based TPMS [80], were found in specimens tested parallel to the build direction. Similar to the density graded lattices this is assumed to stem from the inherent material plasticity of nylon compared to the more brittle metals and could also be influenced by the introduction of fibres to the matrix. However, further investigations are required to shed light on the influence of fibres on the structural response of these lattices.

4.2.2 The effect of grading on the stiffness

By applying the scaling law between the nominal Young's modulus and the relative density of the ungraded baseline lattices, trendlines were generated for both tests conducted parallel and transverse to the build direction, as shown in Fig. 18a). Based on the Eq.7 the total stiffness of the density graded lattices was subsequently determined (see Fig. 18b).

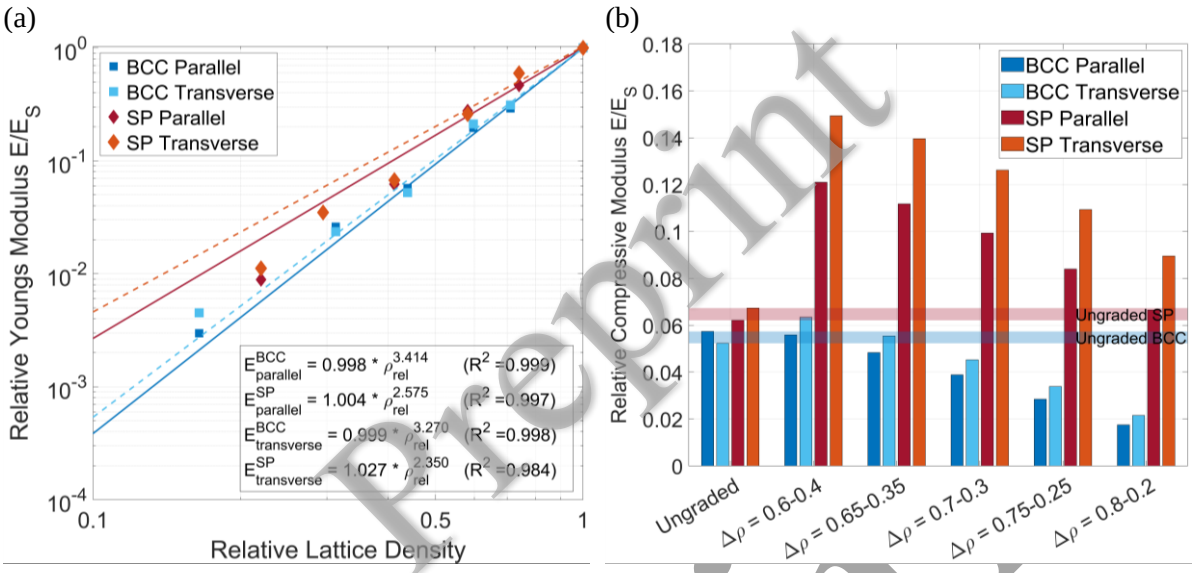

Fig. 18: (a) Fitting of Gibson Ashby model to determine constants of proportionality between relative Young's modulus (modulus of the lattice E divided by the bulk modulus E_S) and the relative lattice density. (b) The relative Young's moduli of the density graded lattices with respect to their ungraded counterparts, as determined from Eq.12.

For the bending-dominated BCC lattices, it is interesting to note, that moderate grading ($\Delta\rho = 0.6 - 0.4$) yields a similar total stiffness compared to the ungraded lattices, whereas more severe grading ($\Delta\rho = 0.8 - 0.3$) gradually reduces the stiffness to ~50% of the ungraded counterpart. On the other hand, the moderately graded stretching-dominated SP lattices display a significant two-fold increase in stiffness and the performance for the most severely graded lattice settles at a similar or even higher value as the uniform lattice for specimens tested parallel and transverse, respectively. The observed effect for moderate grading is in line with the findings illustrated in Fig. 7, demonstrating a threefold increase in stiffness from the lattice with $\rho_{avg} = 0.5$ to $\rho_{avg} = 0.65$, while the stiffness for the lattice with $\rho_{avg} = 0.35$ is only marginally lower than that with $\rho_{avg} = 0.5$. For both the graded BCC and SP lattices, the specimens in transverse to the build direction outperform the once tested parallel to it. This stems from the higher stiffness values obtained from $\rho_{avg} = 0.65$ and $\rho_{avg} = 0.8$ as illustrated in Fig. 7. As these values are derived from the fitted function, it is important to note that they constitute an approximation of the total stiffness and should not be confused with the 'initial' stiffness, which is still governed by the lowest relative density unit cells of the graded lattice.

The different effect of density grading on the bending- and stretching-dominated lattices is shedding light on the importance of establishing baseline values which clearly demonstrate the individual performance of lattices at a given relative density. Therefore, lattices with an even more modest grading between ungraded and 0.6-0.4 could potentially yield an even higher stiffness, providing scope for further fine-tuning. Similarly, knowing to which level the stiffness degrades in comparison to the ungraded counterpart for a given severity of grading is crucial, as it allows e.g. for better tailoring of multi-objective applications such as e.g. local permeability [81] while adhering to a required stiffness value.

From the initial slopes of the load-displacement curves as well as the general curve characteristics of the unit cell size graded lattices (see Fig. 12), it can be concluded, that the elastic and momentary stiffness, respectively, are very similar. Thus, unit cell graded lattices can be tuned to e.g. a specific conductivity rate (possible application for heat sinks) by increasing the surface area per volume through control of the severity of the unit cell size gradient while preserving the stiffness of the structure.

Fig. 19a) illustrates how the ungraded and density graded lattices perform in comparison to the empirical data of Ashby [72]. It was observed, that the data points of the ungraded BCC lattices lie slightly underneath the trendline for an ideal bending-dominated behaviour while having a similar slope, whereas the ungraded SP lattices do not match the ideal stretching-dominated behaviour while showing a slightly steeper trendline than ideally stretching-dominated lattices. With higher relative density both lattice types indicate convergence towards the corresponding ideal behaviour. The graded lattices showcase the potential for fine-tuning the relative stiffness of the lattices, providing a greater spectrum for potential applications. The performance of the SP lattices can be enhanced such that they approximate an ideally bending-dominated behaviour and the moderately graded BCC lattices provide scope for matching the stiffness of a uniform SP lattice of the same density. It is of note, that the differences between those two lattice types are generally small for such a high relative density, but an even greater scope for fine-tuning of the lattice performance through density grading is to be expected for lower relative density lattices.

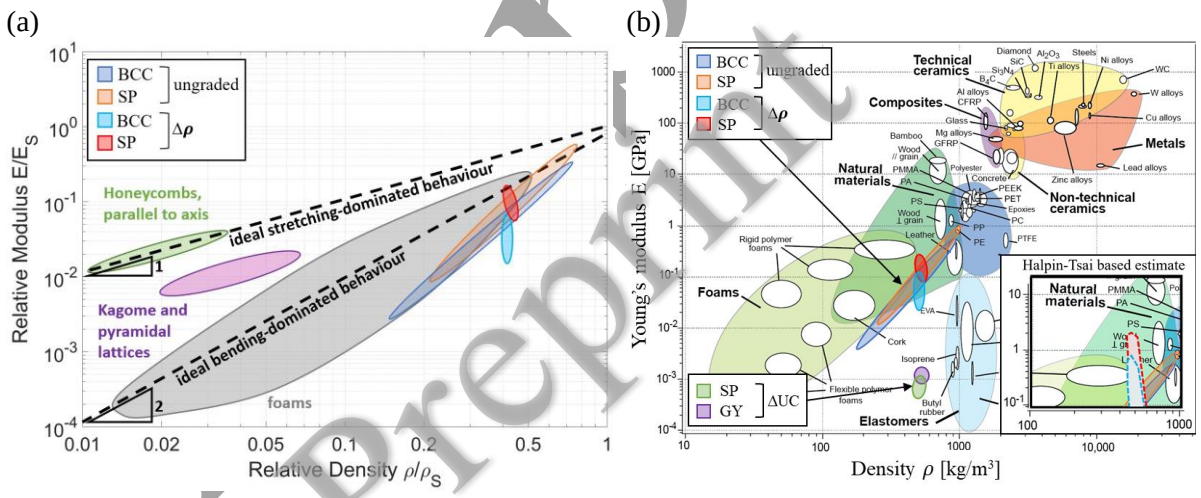

Fig. 19: a) Relative modulus-density curves of bending- and stretching-dominated lattices as redrawn from Ashby [72] (with permission from *The Royal Society*). Included are the values of the ungraded as well as density ($\Delta\rho$) and unit cell size (ΔUC) graded lattices investigated in this study. b) Gibson-Ashby plot, as taken and modified from [82], illustrating the relation between Young's modulus and density for a range of engineering materials and showcasing the nominal compressive moduli of the ungraded and graded lattices investigated in this study as well as the Halpin-Tsai estimated for fibre-volume fraction of ~40%, indicated by the dotted lines.

As shown in Fig. 19b), the stiffness values of the graded and ungraded lattices investigated in this study were integrated into a Gibson-Ashby plot, highlighting their performance with respect to other engineering materials. Interestingly, the density graded

lattices fall into the realm of foams and natural materials, whereas the unit cell size graded lattices behave similarly to elastomers. This insight can inform designers and engineers about the suitability of either density or unit cell graded lattices for their application from a mechanical standpoint but also allows contrasting those with aspects of multi-functionality FGLs have on offer, aiding the decision-making process.

Using the Halpin-Tsai model and the rule of mixture, the specific Young's modulus was included in Fig. 19b) for a fibre volume fraction of 40% instead of ~9%, as determined in [74]. The fibre length and diameter were assumed to be ~7μm and ~100μm, respectively [74,75]. Based on the material data provided by the manufacturer of the filaments [65], it is calculated, that the composite tensile and flexural stiffness increases almost eightfold and more than threefold, respectively. The moduli where hence multiplied by this factor assuming the same relative ratio between the modulus of the lattice and the bulk modulus. This is certainly only an estimate, not considering microstructural or manufacturing aspects and should not be regarded as absolute values but more as an indication. Through a joint optimisation of the mesostructure and the intrinsic material properties a much wider spectrum of specific stiffnesses can eventually be achieved. Thus, the data illustrated in Fig. 19 is intended to serve as an additional insight into potential parameters which can be considered when optimising a design with mechanical and functional behaviour in mind.

4.2.3 The effect of grading on the energy absorption capability

From the graphs in Fig. 20 it can be observed that the SP lattices generally have a greater energy absorption efficiency than the BCC lattices with the same density gradient. In fact, for tests conducted parallel and transverse to the build direction, more severe grading results in an earlier deviation from the initial linear region (mainly dictated by the ungraded lattice) in the BCC lattices. However, this detachment occurs more gradual in the BCC lattices tested transverse to the build direction as opposed to the ones tested parallel to it, suggesting better performance at even lower strains as confirmed in Fig. 11.

It is of note, that the graded SP lattices showcase an efficiency plateau from 25% lattice strain onwards (see Fig. 20), making it potentially very attractive for applications in which a constant material behaviour is desired. It can generally be concluded, that a unique optimum cannot be derived from the efficiency curves of graded lattices and hence there is no clear densification onset strain. This is to be expected, as each individual unit cell layer would be expected to have their own onset strain which is further explaining the load-drops and waviness of the curves. It is overall positive to note how grading results in a constant or increasing efficiency curve, highlighting how these structures can outperform their ungraded counterparts at higher lattice strains (recall Fig. 11) and their scope for tailoring the lattice design to match an envisaged load profile.

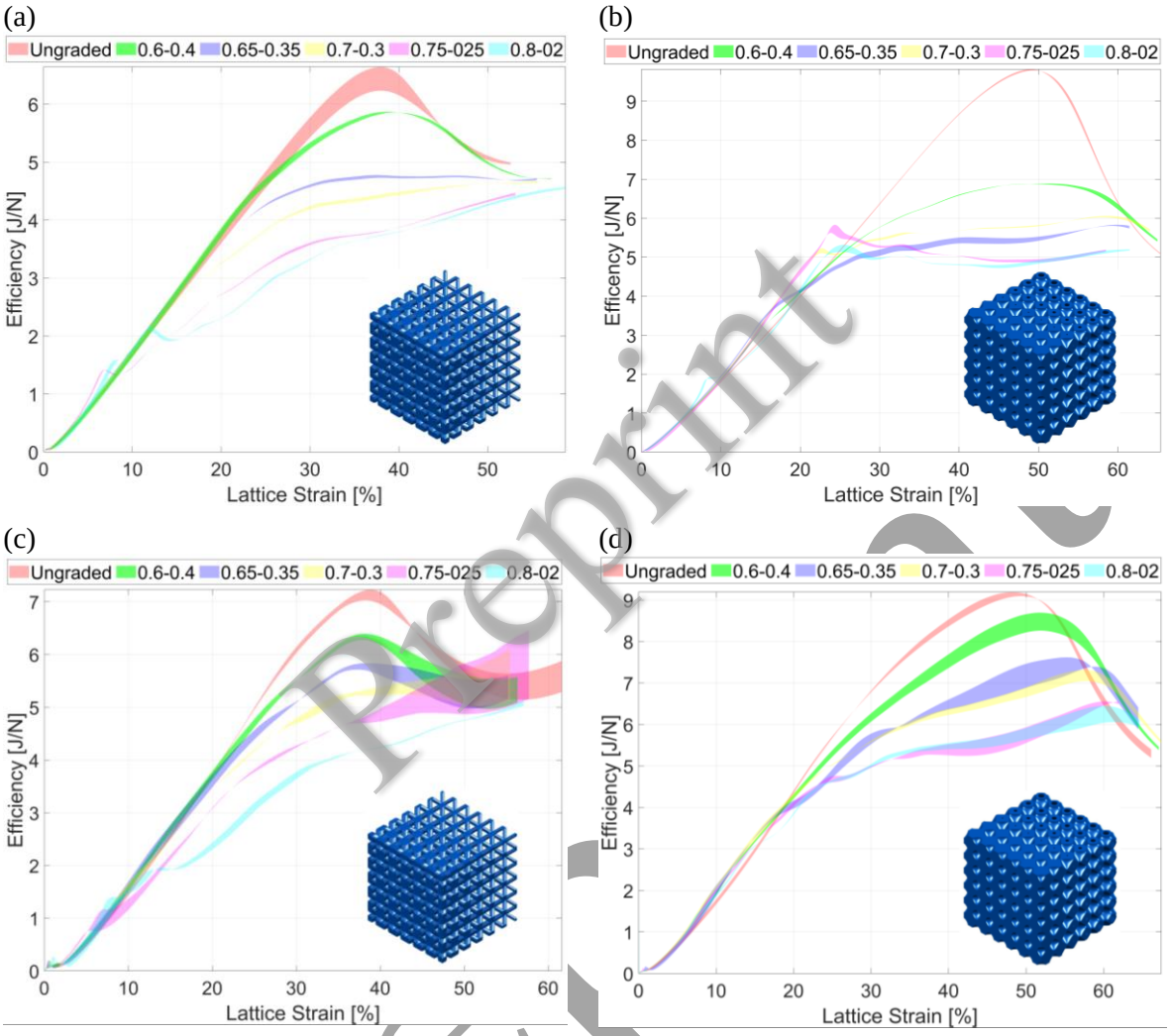

Fig. 20: Efficiency curves for the graded (a)/(c) BCC and (b)/(d) SP lattices compared to the ungraded counterparts with equal mass tested (a)/(b) parallel and (c)/(d) transverse to the build direction.

As proposed by Gibson and Ashby [68], the normalized cumulative energy absorption is plotted over the normalized peak stress (see Fig. 21 & Fig. 22), to better identify lattices which absorb the highest energy at the lowest possible stress. The cumulative energy absorption and peak stress were normalized by the materials Young's modulus E_S. In Fig. 21, the values were displayed together with the envelope curves derived from the five ungraded lattices and plotted as a second-order polynomial.

Typically, a significant increase in energy absorption with a small rise in stress is to be expected in the plateau region (denoted by "B" in Fig. 21) of the ungraded lattices, which can be confirmed by the graphs. In the graded lattices this effect occurs earlier as the layers with a lower theoretical unit cell density of 0.5 have surpassed the yield point already. This has led to significantly better energy absorption capability, particularly in the BCC lattices, prior to the yield stress of the corresponding ungraded equivalent of the same density. In case of the BCC, lattices tested parallel to the build direction, the curves of the most severely graded lattice demonstrate a peak, matching the values of the ungraded envelope curve equivalent to a uniform lattice of lower average density. In turn, it was found that they fail to achieve the same

performance by the onset of densification of the ungraded counterpart. The same effect, although much more muted, was recorded for the graded SP lattices and the curves match the ungraded lattice very well in the corresponding linear-elastic range (see Fig. 21).

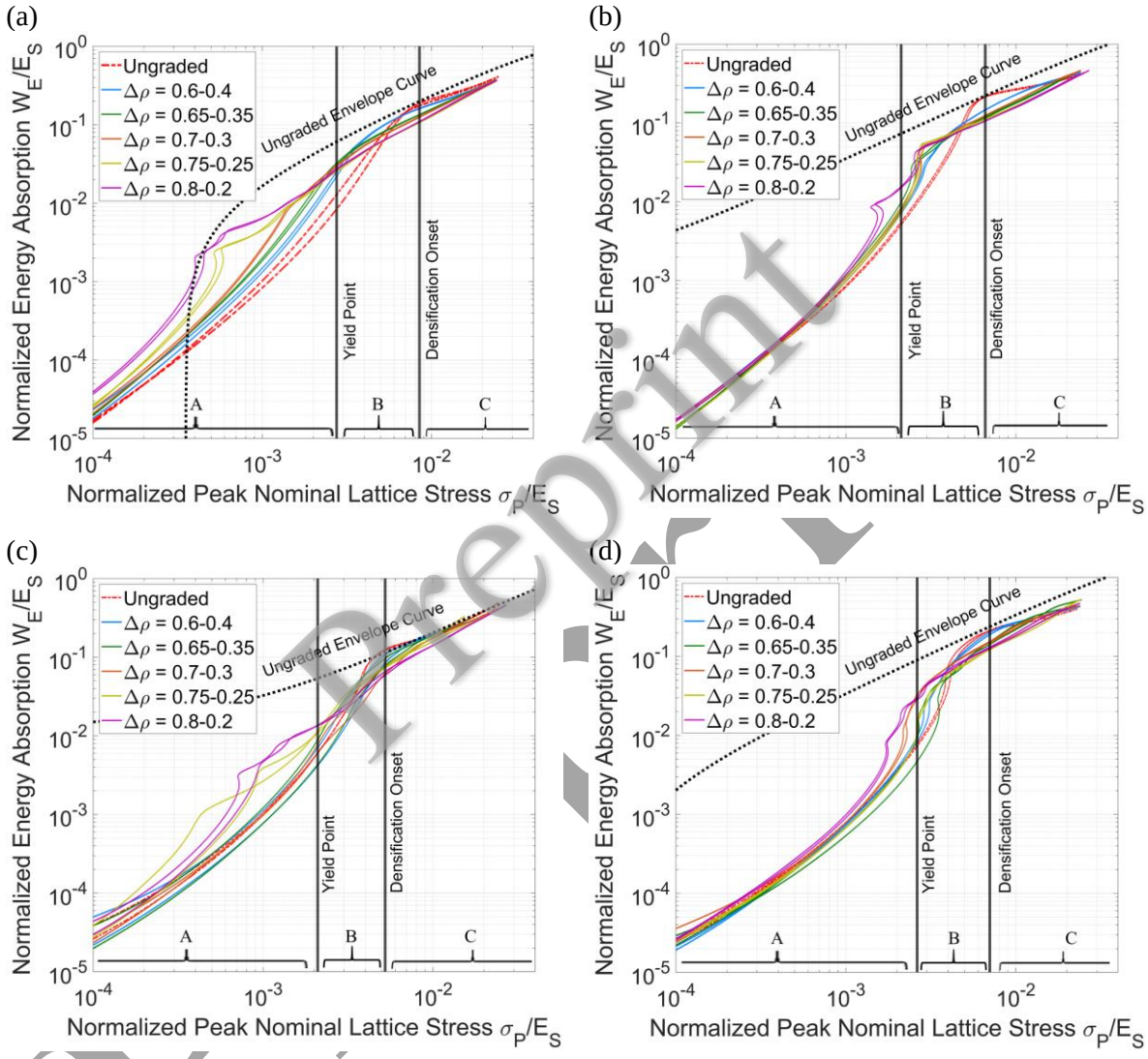

Fig. 21: Normalized nominal energy absorption diagram of the graded (a)/(c) BCC and (b)/(d) SP-lattice tested (a)/(b) parallel and (c)/(d) transverse to the build direction compared to the ungraded counterpart, showing the global response in the elastic realm (A), the plastic yielding corresponding to the plateau region in the load-displacement curve (B) and stress threshold initiating the onset of densification (C). Note that the marked values for the yield and densification onset strain as well as the envelope curve are taken form the ungraded lattice.

It is important to mention, that the abovementioned nominal values must be treated with caution, as the peak stresses are systematically underestimated due to a constant change in the effective surface area through the thickness of the specimen. Hence, Fig. 22 provides further insight into differences between the normalized energy absorption capability at a certain peak unit cell stress for individual unit cell layers in the FGLs. For this purpose, the effective unit cell stress-strain values (stress as load over the effective unit cell area and strain from the optical strain gauge) of the most severely graded lattices were compared to the average effective values

of the ungraded counterpart. It becomes evident, that the graded BCC lattices demonstrate higher energy absorption at lower stresses prior to yielding. Conversely, the SP lattices demonstrate a good agreement with the ungraded counterpart up to yielding with only small peaks prior to that. Hence, grading is only advantageous for BCC lattices if stresses are within the linear-elastic region of the corresponding ungraded lattice with the same relative density.

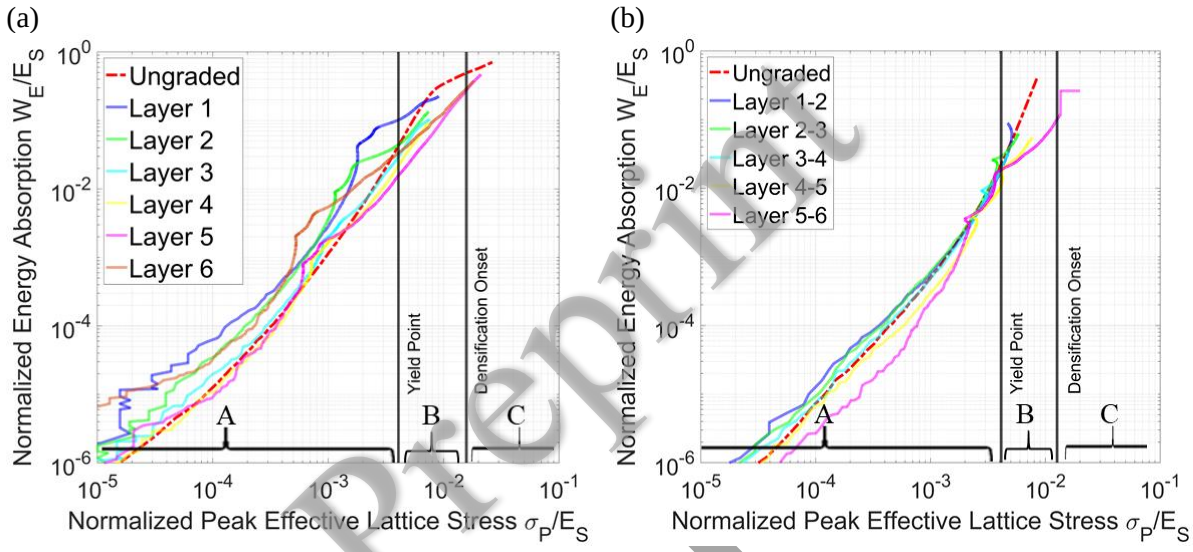

Fig. 22: Normalized effective energy absorption diagram of the most severely graded (a) BCC and (b) SP-lattice (ρ_Δ = 0.8-0.2) tested parallel to the build direction and compared to the ungraded counterpart. Note that these values are directly obtained from the unit cell effective stress-strain values recorded with an optical strain gauge and that the plotted yield and densification onset points are derived from the ungraded lattice of the same density. The regions A, B and C represent the linear-elastic realm, the plateau and the densification region, respectively.

At last Fig. 23 illustrates the normalized nominal energy absorption of the unit cell graded lattices, showcasing no significant differences with respect to either the severity of grading nor the unit cell type. This is in line with the abovementioned results on this family of FGLs. It can, therefore, be concluded that for selecting the correct unit cell type and severity of grading in an AM-design, solely aspects of multi-functionality (e.g. local permeability, etc.) need to be considered as the mechanical performance is equal for lattices with the same relative density. It should be pointed out, that despite the nature-like appearance of these cell-size graded lattices, resembling a hierarchical structure and suggesting - among others - improved energy absorption, this is merely a copy and not a replicate of nature. In fact, the lattice is not strictly a hierarchical configuration but presents only a meso-structure and has at best one second length-scale level (counting the fibre-reinforcement). In addition, it was not actually engineered to replicate the underlying mechanisms (e.g. crack deflection, bridging, interfacial hardening, controlled debonding, etc.) that are pivotal for the superior toughness or energy absorption [83], thus not affecting the performance with change in grading severity.

Overall, these findings can help to better harness the potential of FGLs for specific applications, depending on whether particular stress-constraints (see Fig. 21 - Fig. 23) need to be considered or whether only the cumulative energy absorption is of interest (recall Fig. 11).

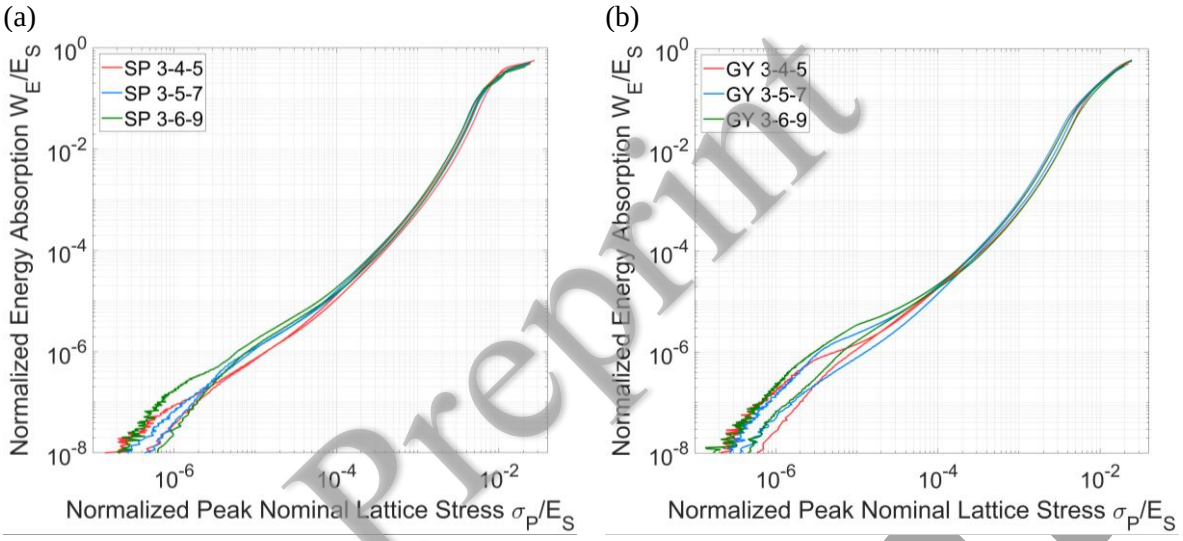

Fig. 23: Normalized nominal energy absorption diagram of the cell size graded (a) SP and (b) GY lattices.

In an attempt to find a semi-empirical formula to predict the cumulative energy absorption behaviour of the lattice types under investigation for a given density gradient and lattice strain, the curves in Fig. 11 were fitted by power-law expressions, providing a goodness-of-fit measure of $R^2 > 0.98$. The average parameters of these initial fits are plotted in Fig. 24 over the density gradient and were subsequently fitted again to derive a trend. This facilitated the determination of the power-law constant and exponent for describing the energy absorption behaviour of the lattices with the same mass for various severities of grading. These consolidated in the following formula:

$$W_{parallel}^{BCC\_0.5} = 1.94\Delta\rho^{-0.46} * \varepsilon_{Latt}^{2.20\Delta\rho+1.99} \quad \text{(Eq.13)}$$

$$W_{parallel}^{SP\_0.5} = 5.96\Delta\rho^{-0.41} * \varepsilon_{Latt}^{1.71\Delta\rho+1.78} \quad \text{(Eq.14)}$$

$$W_{transverse}^{BCC\_0.5} = 8.67\Delta\rho^{-0.03} * \varepsilon_{Latt}^{0.86\Delta\rho+2.21} \quad \text{(Eq.15)}$$

$$W_{transverse}^{SP\_0.5} = 21.4\Delta\rho^{-0.22} * \varepsilon_{Latt}^{1.36\Delta\rho+1.65} \quad \text{(Eq.16)}$$

It is however of note, that the BCC lattices tested transverse to the build direction imply very low accordance with the regression model and therefore should not be considered or needs at least be treated with caution. This stems from the greater variability in the experimental data for this set of specimens as illustrated in Fig. 11 and supports the observations in the deformed specimen that an increased number of cracks have occurred along the print-plane (recall Fig. 16), as the transverse strength of the material is solely governed by the inter-bead bonding strength i.e. the polymer matrix. With the BCC lattice failing in bending this effect is exacerbated, suggesting that the stretching-dominated unit cell types should be favoured to guarantee repeatable performance. Moreover, this sheds light on the importance of optimal processing conditions, allowing sufficient fusion between layers to minimize the occurrence of weak spots aiding the propagation of cracks.

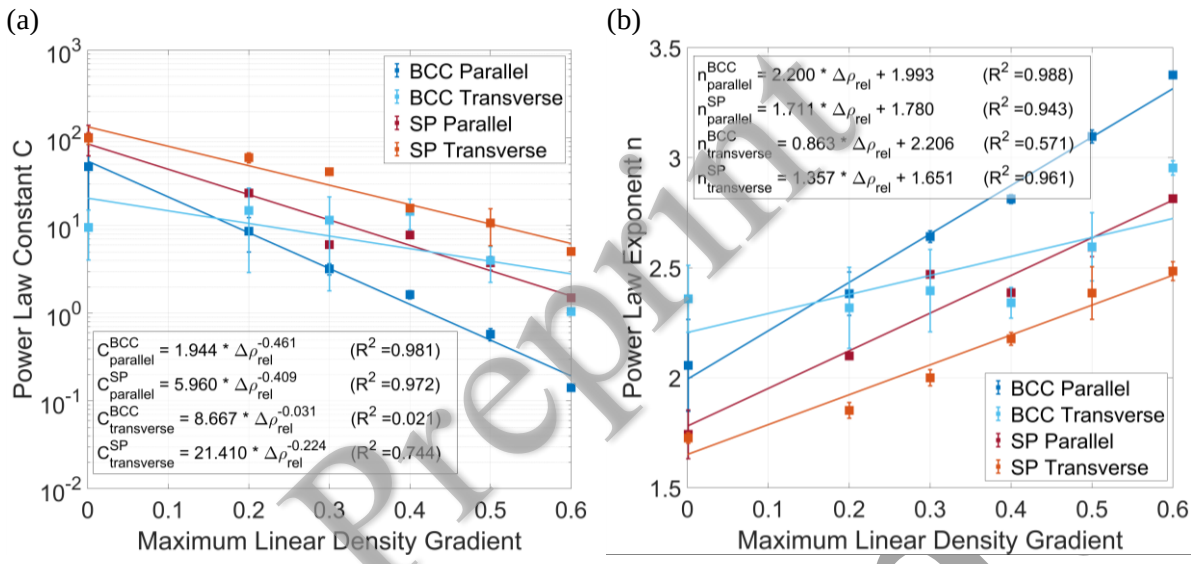

Fig. 24: Average power law constant and exponent derived from a power-law fit for the cummulative energy absorption curves of the density graded lattices. Trendlines of the constants help predict the energy absorption capability as a function of the density gradient, assuming an absorption following the power-law.

The cumulative energy absorption curves of the unit cell size graded lattices were also fitted with a power-law expression, providing an equal goodness-of-fit measure as above. As shown in Fig. 12, no significant differences can be observed between the differently graded lattices, however, a greater variability between equal specimens was observed. For this purpose, the average i.e. mean values are presented in Table 4. Compared to the density graded lattices no distinct trend could be observed. It is however of note that SP lattices with the lowest and the GY with the highest grading severity performed slightly better than the two remaining configurations.

Table 4: Power-law constants of cumulative energy absorption over the lattice strain fit of lattices with different severities of unit cell size gradient. Note *C* is the constant and *m* is the exponent.

$W = C * \varepsilon_{Latt}^{m}$	C_{SP}	C_{GY}	m_{SP}	m_{GY}
3-4-5	173	68	1.67	1.95
3-5-7	**94**	**45**	**1.82**	**2.04**
3-6-9	83	54	1.84	2.03

5 Conclusion

In this article, the effect of the severity of grading on the compressive stiffness, energy absorption and structural response was investigated for additively manufactured short fibre-reinforced functionally graded lattices. The work features both linear unit cell density and unit cell size grading of lattices with the same relative density, composed of Schwarz-P and body-centred-cubic as well as Schwarz-P and Gyroid unit cells, respectively. For the former, baseline values were established from a range of uniform i.e. ungraded lattices, which were utilized to derive and evaluate the properties of the graded counterparts. Besides, all the uniform baseline

and density graded lattices were tested both parallel and transverse to the build direction to provide further insight into manufacturing-related aspects of the performance. In conclusion, mechanical properties and behaviours of the lattices were summarized and embedded into Gibson-Ashby plots providing a categorization of the FGLs. Furthermore, trends with respect to the energy absorption capability for a given density gradient were derived and stiffness estimations with respect to a higher fibre volume fraction centred on the Halpin-Tsai model were provided. In conclusion, the major findings include:

- Moderate grading of the density results in a significantly improved total stiffness of the SP lattices compared to the ungraded counterpart, whereas the BCC lattices yield a similar modulus as the uniform equivalent. In turn, more severe grading results in a reduction in stiffness. This decrease is considerable in the BCC lattice, resulting in a modulus that is only a fraction of the corresponding uniform lattice of same relative density. In contrast, even severely graded SP lattices do not fall below the uniform threshold.
- Specimens tested transverse to the build direction generally showcased a higher variability in performance compared to the ones tested parallel to the build direction. Moreover, it was found, that a higher average lattice density yields greater stiffness values for lattices tested transverse to the build direction. This is assumed to stem from a higher percentage of fibres being orientated favourably, i.e. in 0° and ±45° to the loading direction, thus highlighting the influence of the infill and manufacturing.
- It was found that on average the GY lattices of the same relative density and different severity of unit cell size grading are stiffer than the SP counterparts. No clear trend between the stiffness and the severity of grading was observed for these types of lattices, leading to assume no significant influence of unit cell size grading.
- A categorisation of specific performance of the lattices with respect to the corresponding ideally stretching- and bending-dominated behaviour revealed certainly room for improvement but more importantly highlighted the effect of grading and its potential for fine-tuning the relative modulus for a given density. In comparison to other common engineering materials, both the ungraded and density graded lattices fall in the realm of foams and natural materials, whereas the unit cell size graded lattices can be regarded as elastomeric. An estimate of the stiffness for 40% fibre volume fraction (maximum theoretically achievable with extrusion-based AM) using the Halpin-Tsai model, predicts a three- to eightfold increase.
- The work has highlighted, that a more severe grading has a detrimental effect on the cumulative energy absorption of BCC lattices, whereas, on the contrary, severely graded SP lattices should be favoured for large deformations, beyond the densification onset strain of the corresponding ungraded lattice. However, with respect to the normalized energy absorption for a certain peak stress, it was found, that the density graded BCC lattices outperform the ungraded counterpart up to their respective yield point, while an equal performance was observed for the density graded and ungraded SP lattice.
- The unit cell size graded lattices (SP and GY) showcased almost identical cumulative and normalized energy absorption curves, demonstrating no effect of unit cell type and severity of grading of lattices with same relative density.

- Regarding the failure of the lattices, it was found, that cracks occurred along the print plane, with more severe delaminations for specimens tested transverse to the build direction. Hence, the collected data displays a greater variability for this set of specimens. However, the SP lattices tested parallel to the build direction did not show any visible cracks owing to their stretch-dominated nature. The unit cell size graded lattices exhibited almost exclusively cracks in the region with the largest cell size.
- A semi-empirical formula for the cumulative energy absorption capacity as a function of the density gradient was provided.

This work shall not only inform better AM-designs but is also intended to spark interest for future research on analytical models, capturing the material behaviour of FGLs, which would make a ground-up property prediction and hence design-choices more straight-forward. Further studies into the structural response of both unreinforced and more significantly reinforced lattices (i.e. fibre volume fraction greater than 20%) in conjunction with a consideration of infill patterns and build direction would be a trajectory worthwhile exploring, to fully understand their influence on the performance. Overall, the presented findings highlight the great potential for fibre-reinforced FGLs and help identify key parameters for fine-tuning their performance to better harness the potential AM has on offer for functional lightweight structures.

Acknowledgement

This work was supported and funded by the Department of Aeronautics at Imperial College London and the Engineering and Physical Sciences Research Council (EPSRC) with the project reference number 2091639.

REFERENCES

[1] J. Plocher, A. Panesar, Review on design and structural optimisation in additive manufacturing: Towards next-generation lightweight structures, Mater. Des. 183 (2019) 108164. doi:10.1016/j.matdes.2019.108164.

[2] M. Afshar, A.P. Anaraki, H. Montazerian, et al., Additive manufacturing and mechanical characterization of graded porosity scaffolds designed based on triply periodic minimal surface architectures, J. Mech. Behav. Biomed. Mater. 62 (2016) 481–494. doi:10.1016/j.jmbbm.2016.05.027.

[3] C. Yan, L. Hao, A. Hussein, et al., Ti-6Al-4V triply periodic minimal surface structures for bone implants fabricated via selective laser melting, J. Mech. Behav. Biomed. Mater. 51 (2015) 61–73. doi:10.1016/j.jmbbm.2015.06.024.

[4] D. Mahmoud, M. Elbestawi, Lattice Structures and Functionally Graded Materials Applications in Additive Manufacturing of Orthopedic Implants: A Review, J. Manuf. Mater. Process. 1 (2017) 13. doi:10.3390/jmmp1020013.

[5] L. Zhu, N. Li, P.R.N. Childs, Light-weighting in aerospace component and system design, Propuls. Power Res. 7 (2018) 103–119. doi:10.1016/j.jppr.2018.04.001.

[6] J. Wu, W. Wang, X. Gao, Design and Optimization of Conforming Lattice Structures, (2019) 1–14. http://arxiv.org/abs/1905.02902.

[7] Z. Doubrovski, J.C. Verlinden, J.M.P. Geraedts, Optimal Design for Additive Manufacturing: Opportunities and Challanges, in: Proc. ASME 2011 Int. Des. Eng. Tech. Conf. Comput. Inf. Eng. Conf. IDETC/CIE, Washington, DC, USA, 2011: pp. 1–12.

[8] D. Bourell, J.P. Kruth, M. Leu, et al., Materials for additive manufacturing, CIRP Ann. - Manuf. Technol. 66 (2017) 659–681. doi:10.1016/j.cirp.2017.05.009.

[9] X. Wang, M. Jiang, Z. Zhou, et al., 3D printing of polymer matrix composites: A review and prospective,

Compos. Part B Eng. 110 (2017) 442–458. doi:10.1016/j.compositesb.2016.11.034.
[10] Z. Quan, A. Wu, M. Keefe, et al., Additive manufacturing of multi-directional preforms for composites: Opportunities and challenges, Mater. Today. 18 (2015) 503–512. doi:10.1016/j.mattod.2015.05.001.
[11] P. Parandoush, D. Lin, A review on additive manufacturing of polymer-fiber composites, Compos. Struct. 182 (2017) 36–53. doi:10.1016/j.compstruct.2017.08.088.
[12] B. Brenken, E. Barocio, A. Favaloro, et al., Fused Filament Fabrication of Fiber-Reinforced Polymers: A Review, Addit. Manuf. 21 (2018) 1–16. doi:10.1016/j.addma.2018.01.002.
[13] L.G. Blok, M.L. Longana, H. Yu, et al., An investigation into 3D printing of fibre reinforced thermoplastic composites, Addit. Manuf. 22 (2018) 176–186. doi:10.1016/j.addma.2018.04.039.
[14] T. Hofstätter, D.B. Pedersen, G. Tosello, et al., State-of-the-art of fiber-reinforced polymers in additive manufacturing technologies, J. Reinf. Plast. Compos. 36 (2017) 1061–1073. doi:10.1177/0731684417695648.
[15] H.L. Tekinalp, V. Kunc, G.M. Velez-Garcia, et al., Highly oriented carbon fiber-polymer composites via additive manufacturing, Compos. Sci. Technol. 105 (2014) 144–150. doi:10.1016/j.compscitech.2014.10.009.
[16] F. Ning, W. Cong, J. Qiu, et al., Additive manufacturing of carbon fiber reinforced thermoplastic composites using fused deposition modeling, Compos. Part B Eng. 80 (2015) 369–378. doi:10.1016/j.compositesb.2015.06.013.
[17] M. Ivey, G.W. Melenka, J.P. Carey, et al., Characterizing short-fiber-reinforced composites produced using additive manufacturing, Adv. Manuf. Polym. Compos. Sci. 3 (2017) 81–91. doi:10.1080/20550340.2017.1341125.
[18] J.R. Raney, B.G. Compton, J. Mueller, et al., Rotational 3D printing of damage-tolerant composites with programmable mechanics, in: Proc. Natl. Acad. Sci., 2018: pp. 1–6. doi:10.1073/pnas.1715157115.
[19] B.G. Compton, J.A. Lewis, 3D-printing of lightweight cellular composites, Adv. Mater. 26 (2014) 5930–5935. doi:10.1002/adma.201401804.
[20] Z. Quan, Z. Larimore, A. Wu, et al., Microstructural design and additive manufacturing and characterization of 3D orthogonal short carbon fiber/acrylonitrile-butadiene-styrene preform and composite, Compos. Sci. Technol. 126 (2016) 139–148. doi:10.1016/j.compscitech.2016.02.021.
[21] J.P. Lewicki, J.N. Rodriguez, C. Zhu, et al., 3D-Printing of Meso-structurally Ordered Carbon Fiber/Polymer Composites with Unprecedented Orthotropic Physical Properties, Sci. Rep. 7 (2017) 1–14. doi:10.1038/srep43401.
[22] M. Helou, S. Kara, Design, analysis and manufacturing of lattice structures: an overview, Int. J. Comput. Integr. Manuf. 31 (2017) 243–261. doi:10.1080/0951192X.2017.1407456.
[23] X. Wendy Gu, J.R. Greer, Ultra-strong architected Cu meso-lattices, Extrem. Mech. Lett. 2 (2015) 7–14. doi:10.1016/j.eml.2015.01.006.
[24] M.C. Messner, Optimal lattice-structured materials, J. Mech. Phys. Solids. 96 (2016) 162–183. doi:10.1016/j.jmps.2016.07.010.
[25] X. Wang, T.J. Lu, Optimized acoustic properties of cellular solids, J. Acoust. Soc. Am. 106 (1999) 756–765. doi:10.1121/1.427094.
[26] P. Göransson, Acoustic and vibrational damping in porous solids, Philos. Trans. R. Soc. A Math. Phys. Eng. Sci. 364 (2006) 89–108. doi:10.1098/rsta.2005.1688.
[27] T. Tancogne-Dejean, A.B. Spierings, D. Mohr, Additively-manufactured metallic micro-lattice materials for high specific energy absorption under static and dynamic loading, Acta Mater. 116 (2016) 14–28. doi:10.1016/j.actamat.2016.05.054.
[28] M. Vesenjak, L. Krstulović-Opara, Z. Ren, et al., Cell shape effect evaluation of polyamide cellular structures, Polym. Test. 29 (2010) 991–994. doi:10.1016/j.polymertesting.2010.09.001.
[29] C. Bonatti, D. Mohr, Large deformation response of additively-manufactured FCC metamaterials: From octet truss lattices towards continuous shell mesostructures, Int. J. Plast. 92 (2017) 122–147. doi:10.1016/j.ijplas.2017.02.003.
[30] P. Qiao, M. Yang, F. Bobaru, Impact Mechanics and High-Energy Absorbing Materials: Review, J. Aerosp. Eng. 21 (2008) 235–248. doi:10.1061/(ASCE)0893-1321(2008)21.
[31] L. Cheng, X. Liang, E. Belski, et al., Natural Frequency Optimization of Variable-Density Additive Manufactured Lattice Structure: Theory and Experimental Validation, J. Manuf. Sci. Eng. 140 (2018) 105002. doi:10.1115/1.4040622.
[32] E. Handler, A. Sterling, J. Pegues, et al., Design and Process Considerations for Effective Additive Maufacturing of Heat Exchangers, in: Proc. 28th Annu. Int. Free. Fabr. Symp., Austin (Texas), 2017: pp. 2632–2640.
[33] A.O. Aremu, J. Brennan-Craddock, A. Panesar, et al., A voxel-based method of constructing and skinning conformal and functionally graded lattice structures suitable for additive manufacturing, Addit. Manuf. 13 (2017) 1–13. doi:http://doi.org/10.1016/j.addma.2016.10.006.

[34] H. Wadley, T. Queheillalt, Thermal Applications of Cellular Lattice Structures, Mater. Sci. Forum. 539–543 (2007) 242–247.
[35] L. Cheng, J. Liu, X. Liang, et al., Coupling lattice structure topology optimization with design-dependent feature evolution for additive manufactured heat conduction design, Comput. Methods Appl. Mech. Eng. 332 (2018) 408–439. doi:10.1016/j.cma.2017.12.024.
[36] A. Panesar, M. Abdi, D. Hickman, et al., Strategies for functionally graded lattice structures derived using topology optimisation for Additive Manufacturing, Addit. Manuf. 19 (2018) 81–94. https://doi.org/10.1016/j.addma.2017.11.008.
[37] I. Maskery, A. Hussey, A. Panesar, et al., An investigation into reinforced and functionally graded lattice structures, J. Cell. Plast. 53 (2017) 151–165. doi:10.1177/0021955X16639035.
[38] Architected Materials, NTopology. (2019). https://ntopology.com/architected-materials/ (accessed November 19, 2019).
[39] Altair OptiStruct® Revolutionizes Lattice Structures for 3D Printing, Altair. (2017). http://www.altairhyperworks.com/newsdetail.aspx?news_id=11109&news_country=en-US (accessed December 14, 2017).
[40] Materialise 3-matic Lightweight Structures Module, Materialise. (2017). http://www.materialise.com/en/software/3-matic/modules/lightweight-structures-module (accessed December 14, 2017).
[41] I. Maskery, A.O. Aremu, L. Parry, et al., Effective design and simulation of surface-based lattice structures featuring volume fraction and cell type grading, Mater. Des. 155 (2018) 220–232. doi:10.1016/j.matdes.2018.05.058.
[42] R. Gabbrielli, I.G. Turner, C.R. Bowen, Development of Modelling Methods for Materials to be Used as Bone Substitutes, Key Eng. Mater. 361–363 (2009) 903–906. doi:10.4028/www.scientific.net/kem.361-363.903.
[43] C. Liu, Z. Du, W. Zhang, et al., Additive Manufacturing-Oriented Design of Graded Lattice Structures Through Explicit Topology Optimization, J. Appl. Mech. 84 (2017) 081008. doi:10.1115/1.4036941.
[44] P. Terriault, V. Brailovski, Modeling and simulation of large, conformal, porosity-graded and lightweight lattice structures made by additive manufacturing, Finite Elem. Anal. Des. 138 (2018) 1–11. doi:10.1016/j.finel.2017.09.005.
[45] Y. Wang, L. Zhang, S. Daynes, et al., Design of graded lattice structure with optimized mesostructures for additive manufacturing, Mater. Des. 142 (2018) 114–123. doi:10.1016/j.matdes.2018.01.011.
[46] S. Daynes, S. Feih, W.F. Lu, et al., Optimisation of functionally graded lattice structures using isostatic lines, Mater. Des. 127 (2017) 215–223. doi:10.1016/j.matdes.2017.04.082.
[47] S.Y. Choy, C.N. Sun, K.F. Leong, et al., Compressive properties of functionally graded lattice structures manufactured by selective laser melting, Mater. Des. 131 (2017) 112–120. doi:10.1016/j.matdes.2017.06.006.
[48] D.S.J. Al-Saedi, S.H. Masood, M. Faizan-Ur-Rab, et al., Mechanical properties and energy absorption capability of functionally graded F2BCC lattice fabricated by SLM, Mater. Des. 144 (2018) 32–44. doi:10.1016/j.matdes.2018.01.059.
[49] M. Afshar, A. Pourkamali Anaraki, H. Montazerian, Compressive characteristics of radially graded porosity scaffolds architectured with minimal surfaces, Mater. Sci. Eng. C. 92 (2018) 254–267. doi:10.1016/j.msec.2018.06.051.
[50] S. Wang, J. Wang, Y. Xu, et al., Compressive behavior and energy absorption of polymeric lattice structures made by additive manufacturing, Front. Mech. Eng. (2019). doi:10.1007/s11465-019-0549-7.
[51] I. Maskery, N.T. Aboulkhair, A.O. Aremu, et al., A mechanical property evaluation of graded density Al-Si10-Mg lattice structures manufactured by selective laser melting, Mater. Sci. Eng. A. 670 (2016) 264–274. doi:10.1016/j.msea.2016.06.013.
[52] D. Li, W. Liao, N. Dai, et al., Comparison of Mechanical Properties and Energy Absorption of Sheet-Based and Strut-Based Gyroid Cellular Structures with Graded Densities, Materials (Basel). 12 (2019). doi:doi:10.3390/ma12132183.
[53] C. Han, Y. Li, Q. Wang, et al., Continuous functionally graded porous titanium scaffolds manufactured by selective laser melting for bone implants, J. Mech. Behav. Biomed. Mater. 80 (2018) 119–127. doi:10.1016/j.jmbbm.2018.01.013.
[54] J. Kadkhodapour, H. Montazerian, S. Raeisi, Investigating internal architecture effect in plastic deformation and failure for TPMS-based scaffolds using simulation methods and experimental procedure, Mater. Sci. Eng. C. 43 (2014) 587–597. doi:10.1016/j.msec.2014.07.047.
[55] L. Yang, R. Mertens, M. Ferrucci, et al., Continuous graded Gyroid cellular structures fabricated by selective laser melting: Design, manufacturing and mechanical properties, Mater. Des. 162 (2019) 394–404. doi:10.1016/j.matdes.2018.12.007.
[56] H. Montazerian, M.G.A. Mohamed, M.M. Montazeri, et al., Permeability and mechanical properties of

gradient porous PDMS scaffolds fabricated by 3D-printed sacrificial templates designed with minimal surfaces, Acta Biomater. 96 (2019) 149–160. doi:10.1016/j.actbio.2019.06.040.

[57] S. Li, S. Zhao, W. Hou, et al., Functionally Graded Ti-6Al-4V Meshes with High Strength and Energy Absorption, Adv. Eng. Mater. 18 (2016) 34–38. doi:10.1002/adem.201500086.

[58] N. Yang, Z. Quan, D. Zhang, et al., Multi-morphology transition hybridization CAD design of minimal surface porous structures for use in tissue engineering, CAD Comput. Aided Des. 56 (2014) 11–21. doi:10.1016/j.cad.2014.06.006.

[59] D.J. Yoo, K.H. Kim, An advanced multi-morphology porous scaffold design method using volumetric distance field and beta growth function, Int. J. Precis. Eng. Manuf. 16 (2015) 2021–2032. doi:10.1007/s12541-015-0263-2.

[60] F. Liu, Z. Mao, P. Zhang, et al., Functionally graded porous scaffolds in multiple patterns: New design method, physical and mechanical properties, Mater. Des. 160 (2018) 849–860. doi:10.1016/j.matdes.2018.09.053.

[61] Islam M. El-Galy, Bassiouny I. Saleh, Mahmoud H. Ahmed, Functionally graded materials classifications and development trends from industrial point of view, SN Appl. Sci. 1 (2019) 1378–1401. doi:https://doi.org/10.1007/s42452-019-1413-4.

[62] D. Bhate, C. Penick, L. Ferry, et al., Classification and Selection of Cellular Materials in Mechanical Design: Engineering and Biomimetic Approaches, Designs. 3 (2019) 19. doi:10.3390/designs3010019.

[63] D. Bhate, Four questions in cellular material design, Materials (Basel). 12 (2019). doi:10.3390/ma12071060.

[64] J. Plocher, A. Panesar, Mechanical Performance of Additively Manufactured Fiber-Reinforced Functionally Graded Lattices, JOM. (2019). doi:10.1007/s11837-019-03961-3.

[65] Composite 3D Printing, Markforged, Inc. (2017). https://markforged.com/composites/ (accessed December 14, 2017).

[66] I. Maskery, A.O. Aremu, L. Parry, et al., Effective design and simulation of surface-based lattice structures featuring volume fraction and cell type grading, Mater. Des. 155 (2018) 220–232. doi:10.1016/j.matdes.2018.05.058.

[67] I. Maskery, L. Sturm, A.O. Aremu, et al., Insights into the mechanical properties of several triply periodic minimal surface lattice structures made by polymer additive manufacturing, Polymer (Guildf). 152 (2018) 62–71. doi:10.1016/j.polymer.2017.11.049.

[68] I. Gibson, M. Ashby, Cellular Solids: Structure and Properties - Second Edition, 2nd ed., Cambridge University Press, Cambridge, 1997. doi:10.1017/CBO9781139878326.

[69] J.C. Halpin, J.L. Kardos, The Halpin-Tsai Equations : A Review, Polym. Eng. Sci. 16 (1976) 344–352.

[70] R. Matsuzaki, M. Ueda, M. Namiki, et al., Three-dimensional printing of continuous-fiber composites by in-nozzle impregnation, Sci. Rep. 6 (2016) 1–7. doi:10.1038/srep23058.

[71] Q.M. Li, I. Magkiriadis, J.J. Harrigan, Compressive strain at the onset of densification of cellular solids, J. Cell. Plast. 42 (2006) 371–392. doi:10.1177/0021955X06063519.

[72] M.F. Ashby, The properties of foams and lattices, Philos. Trans. R. Soc. A Math. Phys. Eng. Sci. 364 (2006) 15–30. doi:10.1098/rsta.2005.1678.

[73] Markforged Material Datasheet - Composites, Markforged, Inc. (2018). https://static.markforged.com/markforged_composites_datasheet.pdf (accessed May 14, 2019).

[74] M.J. Sauer, Evaluation of the Mechanical Properties of 3D Printed Carbon Fiber Composites, 2018. https://openprairie.sdstate.edu/etd/2436.

[75] J. Naranjo-Lozada, H. Ahuett-Garza, P. Orta-Castañón, et al., Tensile properties and failure behavior of chopped and continuous carbon fiber composites produced by additive manufacturing, Addit. Manuf. 26 (2019) 227–241. doi:10.1016/j.addma.2018.12.020.

[76] T. Isobe, T. Tanaka, T. Nomura, et al., Comparison of strength of 3D printing objects using short fiber and continuous long fiber, IOP Conf. Ser. Mater. Sci. Eng. 406 (2018). doi:10.1088/1757-899X/406/1/012042.

[77] C. Casavola, A. Cazzato, V. Moramarco, et al., Orthotropic mechanical properties of fused deposition modelling parts described by classical laminate theory, Mater. Des. 90 (2016) 453–458. doi:10.1016/j.matdes.2015.11.009.

[78] Sugavaneswaran M. and Arumaikkannu G., Additive manufactured multi-material structure with directional specific mechanical properties based upon classical lamination theory, (2018). doi:10.1108/RPJ-06-2017-0118.

[79] C. Yan, L. Hao, A. Hussein, et al., Evaluations of cellular lattice structures manufactured using selective laser melting, Int. J. Mach. Tools Manuf. 62 (2012) 32–38. doi:10.1016/j.ijmachtools.2012.06.002.

[80] O. Al-ketan, D. Lee, R. Rowshan, et al., Functionally Graded and Multi-Morphology Sheet TPMS, J. Mech. Behav. Biomed. Mater. (2019) 103520. doi:10.1016/j.jmbbm.2019.103520.

[81] J. Plocher, C. Lee, A. Panesar, Additive Manufacturing of Bone-Inspired Structural Power Composites,

in: 22nd Int. Conf. Compos. Mater., Melbourne, 2019.
[82] Material property charts, Granta Des. (2019). https://grantadesign.com/education/students/charts/ (accessed November 10, 2019).
[83] A.R. Studart, Towards high-performance bioinspired composites, Adv. Mater. 24 (2012) 5024–5044. doi:10.1002/adma.201201471.